UNIVERSIDADE D
COIMBRA

Ana Beatriz Guerra Lopes

Residual Stresses in Metal Additive Manufacturing

Dissertation to obtain a Master's Degree in Physical Engineering, specialisation in Metrology and Quality, supervised by Prof. Doutora Maria José Fernandes Vaz Lourenço Marques and by Prof. Doutor António Adriano Castanhola Batista and presented to the Physics Department of the Faculty of Science and Technology of the University of Coimbra.

October 2021

FACULDADE DE CIÊNCIAS E TECNOLOGIA
UNIVERSIDADE D COIMBRA

Residual Stresses in Metal Additive Manufacturing

Dissertation presented to the University of Coimbra in fulfilment of the requirements necessary to obtain a Master degree in Physical Engineering, specialisation in Metrology and Quality.

Ana Beatriz Guerra Lopes

Supervisors: Prof. Dra. Maria José F. V. L. Marques University of Porto
Prof. Dr. António A. Castanhola Batista University of Coimbra

October 2021

Abstract

Selective laser melting (SLM) is a powder bed based additive manufacturing (AM) process and is one of the most established techniques applied in the fabrication of functional parts from metal powders. However, one of the problems with its application in the industry is the presence of residual stresses. These are a consequence of the high temperature gradients and the densification ratio, both of which are innate of this process.

The experimental work developed in this dissertation had the goal of characterising SLM samples produced with two different materials (AISI 18Ni300 and AISI 316L) and with different geometries. A microstructural characterization was made and for the AISI 18Ni300 a study on the quantification of retained austenite was done. The analysis of the residual stresses was made through X-ray diffraction and incremental hole drilling methods. This analysis was made with samples still connected to the metallic build plate and after the removal of the samples from the metallic build plate.

In the study of the residual stresses at the surface, for the AISI 316L only tensile residual stress values were recorded, while for the AISI 18Ni300 the top surface has tensile residual stresses but, on the lateral surfaces and the bases the residual stresses are mostly compressive. In-depth, the residual stress distribution determined by the two methods, only shows tensile residual stress values for the AISI 316L, while, for the AISI 18Ni300 both compressive and tensile residual stress values were determined.

Keywords: X-ray diffraction, AISI 18Ni300, AISI 316L, Incremental hole drilling method, Additive manufacturing

Resumo

A fusão seletiva a laser (SLM) é uma das mais usadas técnicas de fabrico aditivo de peças metálicas. A nível industrial a sua aplicação é ainda limitada devido aos elevados gradientes de temperatura e densificação limitada, que levam ao aparecimento de tensões residuais.

Nesta dissertação foram analisadas amostras produzidas por SLM, com dois materiais diferentes (aço maraging AISI 18NI300 e aço inoxidável austenítico AISI 316L) e com geometrias diferentes. Além da caracterização microestrutural das amostras procedeu-se à análise do estado de tensões residuais na superfície e no interior das amostras, usando a técnica de difração de raios X e o método do furo incremental. Esta análise foi efetuada em dois momentos distintos, após a produção das peças, quando elas ainda se encontravam ligadas ao tabuleiro metálico onde foram produzidas, e após a sua separação do tabuleiro. Procedeu-se também à quantificação do teor de austenite residual nas amostras de aço maraging.

No estudo da distribuição de tensões residuais na superfície das amostras, para o aço AISI 316L apenas se registaram valores de tensões residuais de tração, enquanto para o aço AISI 18Ni300 na superfície do topo da amostra as tensões residuais são de tração, mas nas superfícies laterais e nas bases existem valores de tensões residuais de compressão. Em profundidade, as tensões residuais determinadas para o aço AISI 316L apresentam valores de tensões residuais de tração, enquanto que para o aço AISI 18Ni300 determinaram-se valores de tensões residuais de compressão e de tração.

Palavras-Chave: Difração de raios X, AISI 18Ni300, AISI 316L, Método do furo incremental, Fabrico aditivo

O valor das coisas não está no tempo que elas duram, mas na intensidade com que acontecem.
Por isso existem momentos inesquecíveis, coisas inexplicáveis e pessoas incomparáveis

Fernando Pessoa

Acknowledgements

Firstly, I would like to express my gratitude to all who have contributed to completing this project.

I would like to thank my supervisors, Prof. Doutora Maria José Marques from the University of Porto and Prof. Doutor António Castanhola from the University of Coimbra, for their guidance and valuable input during the project. I am thankful to Prof. Doutor João Paulo Nobre from the University of Coimbra, who helped on the experimental part of the incremental hole drilling method.

Finally, I want to express my profound gratitude to my parents who have offered constant support and encouragement, directly and indirectly, throughout this degree and while writing this dissertation. In particular to my father for the time and patience he gave me.

This work was supported:

- by FEDER, through the Programa Operacional Factores de Competitividade - COMPETE and by national funds through FCT - Fundação para a Ciência e a Tecnologia in the frame of project Projeto POCI-01-0145-FEDER-031895, "MAMTool - Maquinabilidade de components produzidos por fabricação aditiva para a indústria dos moldes";
- by national funds through FCT - Fundaçao para a Ciência e a Tecnologia, I.P., within the projects UIDB/04564/2020 and UIDP/04564/2020.

Contents

List of Abbreviations **xiii**

List of Figures **xv**

List of Tables **xix**

1 Introduction **1**
1.1 Framework and Motivation . . . 1
1.2 Objective . . . 1
1.3 Outline . . . 2

2 State of the Art **3**
2.1 Additive manufacturing . . . 3
2.1.1 Introduction to additive manufacturing . . . 3
2.1.2 Additive manufacturing processes . . . 4
2.1.3 Metal additive manufacturing . . . 5
2.2 Selective Laser Melting . . . 5
2.2.1 SLM process . . . 6
2.2.2 Process parameters . . . 7
2.2.3 Shortcomings of SLM . . . 9
2.3 Maraging steel - AISI 18Ni300 . . . 11
2.3.1 Strengthening mechanisms . . . 11
2.3.2 Maraging steel in AM . . . 11
2.4 Stainless steel - AISI 316L . . . 12
2.5 Residual Stresses . . . 12
2.5.1 Residual stresses in SLM . . . 13

3 Materials and Methods **15**
3.1 Materials . . . 15
3.2 Phase identification by X-Ray diffraction . . . 17
3.3 Quantification of austenite on maraging steel samples . . . 17
3.4 Residual stresses determination by X-ray diffraction . . . 19
3.5 Residual stresses determination by Incremental hole drilling . . . 22
3.6 Metallographic analysis . . . 24
3.6.1 Sample preparation . . . 24
3.7 Microhardness test . . . 26
3.8 Optical microscopy . . . 26

4 Results and discussion **27**
4.1 Phase identification 27
4.2 Quantification of retained austenite in the Maraging Steel samples 28
4.3 Metallographic analysis 28
4.4 Microhardness test 30
4.5 Residual Stresses 31
4.5.1 Surface residual stresses on samples connected to the build plate 31
4.5.2 Surface residual stresses after sample removal from the build plate 35
4.5.3 In-depth residual stresses on samples connected to the build plate 39
4.5.4 In-depth residual stresses after sample removal from the build plate . . . 41

5 Conclusions and Future Work **45**
5.1 Conclusions 45
5.2 Future Work 46

A Appendix Title **47**
A.1 Residual Stresses 47
A.1.1 Surface residual stresses of the AISI 18Ni300 maraging steel sample MAR_T 47
A.1.2 Surface residual stresses of the AISI 18Ni300 maraging steel sample MAR_0 48
A.1.3 Surface residual stresses of the AISI 316L stainless steel sample SS_02 . . 51

List of Abbreviations

3D	Three Dimensional
AM	Additive Manufacturing
ASTM	American Society for Testing and Materials
CAD	Computer-aided Design
IHD	Incremental Hole Drilling
ISO	International Organization for Standardization
LOF	Lack-of-fusion
MAM	Metal Additive Manufacturing
RP	Rapid Prototyping
SLM	Selective Laser Melting
TGM	Temperature Gradient Mechanism
XRD	X-Ray Diffraction

List of Figures

2.1 Benefits (++) and weaknesses (−−) of additive manufacturing processes compared to traditional manufacturing processes [3] 4
2.2 Potential benefits of AM application fields from an environmental perspective [3]. 4
2.3 Selective Laser Melting process, [4] 6
2.4 The most influential process parameters that affect the quality of a part processed by SLM [4] 7
2.5 SLM process parameters: laser power, scanning speed, hatch/scan spacing, and layer thickness [10]. 7
2.6 Solidification phenomenon during SLM: (a) partially penetration of laser into powder bed, (b) adequate laser penetration into powder layer [2] 8
2.7 Effect schematic of scanning space/hatch on forming parts: (a) is too small; (b) is too large [8]. 8
2.8 Scan Patterns: a) Unidirectional and b) Bi-directional. Adapted from [4]. 9
2.9 Scan pattern checkerboard. Adapted from [4]. 9
2.10 The influence of the scan speed on the porosity: a) 250 mm/s, b) 500 mm/s, c) 750 mm/s, and d) 1000 mm/s [15]. 10
2.11 Lack-of-fusion defects: a) Poor bonding defects, b) Unmelted powders [17]. . . . 10
2.12 Definition of residual stresses (Type I, II, III) for a biphasic material [29]. 13
2.13 Variation of residual stress magnitude with laser power and scanning speed for Maraging Steel 300 [30]. 13
2.14 TGM inducing residual stresses: (a) when heating and (b) during cooling (plastic ε_{pl} and thermal elongation ε_{th}, tensile σ_{tens} and compressive σ_{comp} stress) [29]. . 14
2.15 Cool-down phase inducing residual stress at solid layer connection (a) when heating, (b) during cooling [29]. 14

3.1 Samples: (a) MAR_T, (b) MAR_0, (c) SS_T2 and (d) SS_02. 16
3.2 X-Ray diffraction equipment's used: (a) Seifert XRD 3000 PTS and (b) Proto iXRD portable diffractometer. 16
3.3 **L** is the laboratory referential, related to the diffraction conditions. **P** is the sample referential. σ_Φ is the stress direction of interest. 20
3.4 (a) Schematic representation of the referential used during the study of the samples (b) Nomenclature of different samples surfaces. 21
3.5 (a) Proto Electrolytic Polisher, model 8818 and (b) The Top face of the SS_T2 sample after the electrolytic polishing method. 22

3.6 Incremental Hole Drilling: (a) Schematic Geometry of a Typical Three-Element Clockwise (CW) Hole-Drilling Rosette, (b) Hole Geometry and Residual Stresses for non-uniform stresses where D is the diameter of the gage circle and D_0 is the diameter of the drilled hole [32] and (c) Vishay RS 200 milling guide connected to a HBM Spider 8-30 DAQ system at the GTR lab. 24
3.7 Schematic representation of holes drilled and their nomenclature (a) before the removal of the build plate and (b) after the removal of the build plate. 24
3.8 Schematic of the sectioning of the samples MAR_0 and SS_T2. 25
3.9 Four-Step polishing procedure used to polish samples [33]. 25
3.10 Equipment used for the preparation of samples for the microstructural analysis: (a) Struers Labotom used for the sectioning of the samples (b) Struers Prestopress - 3 used for the capsuling of the samples (c) Struers Planopol/Pedemax 2 used to polish the samples. 25
3.11 Vickers Microhardness method and equipment: (a) Schematic of the Vickers Microhardness method test, [35] (b) Shimadzu Microhardness tester, type-M, used for the Vickers Microhardness tests. 26

4.1 Diffractograms: (a) AISI 18Ni300 and (b) AISI 316L. 27
4.2 Schematic representation of the analysed sections. 29
4.3 Microstructure obtained through optical microscopy on the XY cross section: (a) and (b) AISI 18Ni300 maraging steel; (c) and (d) AISI 316L stainless steel. . 29
4.4 Microstructure obtained through optical microscopy on the YZ cross section: (a) and (b) AISI 18Ni300 maraging steel; (c) and (d) AISI 316L stainless steel. In (b) the circles identify the martensitic needles. 30
4.5 Residual stresses on the sample MAR_T while still connected to the build plate: (a) top surface σ_{xx} (b) top surface σ_{yy} (c) lateral surface σ_{xx} (d) lateral surface σ_{zz} (e) base surface σ_{zz} (f) base surface σ_{yy} 32
4.6 Residual stresses on the sample SS_T2 while still connected to the build plate: (a) top surface σ_{xx} (b) top surface σ_{yy} (c) lateral surface σ_{xx} (d) lateral surface σ_{zz} (e) base surface σ_{zz} (f) base surface σ_{yy}. 34
4.7 Residual stresses on the sample MAR_T without the build plate: (a) top surface σ_{xx} (b) top surface σ_{yy} (c) lateral surface σ_{xx} (d) lateral surface σ_{zz} (e) base surface σ_{zz} (f) base surface σ_{yy}. 36
4.8 Residual stresses on the sample SS_T2 without the build plate: (a) top surface σ_{xx} (b) top surface σ_{yy} (c) lateral surface σ_{xx} (d) lateral surface σ_{zz} (e) base surface σ_{zz} (f) base surface σ_{yy}. 38
4.9 In-depth analysis of the residual stresses in the MAR_T sample using the incremental hole drilling method: (a) top surface σ_{xx} (b) top surface σ_{yy} (c) lateral surface σ_{xx} (d) lateral surface σ_{zz}. 39
4.10 In-depth analysis of the residual stresses in the SS_T2 sample using the incremental hole drilling method: (a) top surface σ_{xx} (b) top surface σ_{yy} (c) lateral surface σ_{xx} (d) lateral surface σ_{zz}. 40
4.11 Residual stresses in-depth analysis, by XRD and by IHD in the MAR_T sample: (a) top surface σ_{xx} (b) top surface σ_{yy} (c) lateral surface σ_{xx} (d) lateral surface σ_{zz}. 42
4.12 Residual stresses in-depth analysis, by XRD and by IHD in the SS_T2 sample: (a) top surface σ_{xx} (b) top surface σ_{yy} (c) lateral surface σ_{xx} (d) lateral surface σ_{zz}. 43

A.1 Residual stresses on the sample MAR_T before build plate removal: (a) Lateral surface σ_{xx} (b) Lateral surface σ_{zz} 47
A.2 Residual stresses on the sample MAR_T after build plate removal: (a) Lateral surface σ_{xx} (b) Lateral surface σ_{zz} 48
A.3 Residual stresses on the sample MAR_0 before build plate removal: (a) Top surface σ_{xx} and σ_{yy} (b) Lateral surface σ_{xx} (c) Lateral surface σ_{zz} (d) Base surface σ_{zz} and σ_{yy} 49
A.4 Residual stresses on the sample MAR_0 after build plate removal: (a) Top surface σ_{xx} and σ_{yy} (c) Lateral surface σ_{xx} (d) Lateral surface σ_{zz} (e) Base surface σ_{zz} and σ_{yy} 50
A.5 Residual stresses on the sample SS_02 before build plate removal: (a) top surface σ_{xx} and σ_{yy} (b) lateral surface Frontal 2 σ_{xx} (c) lateral surface Frontal 2 σ_{zz} . . 51
A.6 Residual stresses on the sample SS_02 before build plate removal: (a) lateral surface Frontal 1 σ_{xx} (b) lateral surface Frontal 1 σ_{zz} (c) base surface σ_{zz} and σ_{yy} 52
A.7 Residual stresses on the sample SS_02 after build plate removal: (a) top surface σ_{xx} and σ_{yy} (b) lateral surface Frontal 2 σ_{xx} (c) lateral surface Frontal 2 σ_{zz} . . 53
A.8 Residual stresses on the sample SS_02 after build plate removal: (a) lateral surface Frontal 1 σ_{xx} (b) lateral surface Frontal 1 σ_{zz} (c) base surface σ_{zz} and σ_{yy} 54

List of Tables

3.1 Chemical Composition Limits of 18Ni-300 maraging steel [22]. 15
3.2 Chemical Composition Limits of AiSi 316 L Stainless Steel [26]. 15
3.3 SLM process parameters for the AISI 18Ni300 maraging steel and the AISI 316L stainless steel given by the supplier [22, 26]. 15
3.4 Sample dimensions. 16
3.5 Acquisition parameters for phase identification. 17
3.6 Acquisition parameters for the retained austenite quantification with Cu-Kα radiation used in the Seifert XRD 3000 PTS diffractometer, where A is Austenite and M is Martensite. 18
3.7 Acquisition parameters for the retained austenite quantification with Cr-Kα radiation used in the Proto iXRD diffractometer, where A is Austenite and M is Martensite. 19
3.8 Acquisition parameters used for each material in residual stresses determination by X-ray diffraction with the Proto iXRD diffractometer. 21
3.9 Mechanical properties of both materials and the rosettes used in the Incremental hole drilling. 24

4.1 Retained austenite percentage in the AISI 18Ni300 samples obtained with the Seifert diffractometer with Cu-Kα radiation. 28
4.2 Retained austenite percentage in the AISI 18Ni300 samples obtained with the Proto diffractometer with Cr-Kα radiation. 28
4.3 Test parameters used for each material in the Vickers microhardness test. . . . 30
4.4 Vickers microhardness test results for the AISI 316L sample. 30
4.5 Vickers microhardness test results for the AISI 18Ni300 sample. 31
4.6 In sample positioning of the points where the analysis to determine the residual stresses by XRD method was made (Section 3.4). 41
4.7 In sample positioning of the points where the analysis to determine the residual stresses by IHD method was made (Section 3.4). 41

Chapter 1

Introduction

1.1 Framework and Motivation

This work is part of the cross-disciplinary project MAMTool - Machinability of Additive Manufactured Parts for Tooling Industry - currently being developed at INEGI/FEUP, CFisUC and IDMEC/IST. This project focus on the machining behaviour of metallic powder-based melting additive manufactured tool components and has as its goal the development of numerical predictive tools to simulate the metal cutting mechanics accounting for the specification of Additive Manufacturing materials.

Additive Manufacturing is the colloquial terminology of processes that facilitate complex 3D structures to be created through the addition of material instead of its subtraction. Typically, the addition of material is made layer by layer. This approach allows 3D models to be created, opening the world to more complex designs. However, new physical and mechanical aspects are a consequence of this type of process.

The objective of this dissertation was studying the characterisation of samples of AISI 18Ni300 maraging steel and AISI 316L stainless steel after being produced by additive manufacturing. The X-Ray diffraction technique will be used to quantify the amount of retained austenite and to determine the residual stresses. The in-depth residual stress distribution will be analysed by the X-Ray Diffraction and the Hole Drilling methods. The microstructure of the samples will be characterised by optical microscopy and its micro-hardness will also be analysed.

1.2 Objective

The main purpose of this work was to characterise the mechanical properties of metallic parts elaborated by the additive manufacturing process SLM (Selective Laser Melting). The results obtained will be used in the validation of a finite element model being developed simultaneously within the scope of the project in which this work is included.

1.3 Outline

This work is divided in five parts:

- Chapter 1 - Introduction: The presentation of the motivation, framework, objectives and outline of this work.
- Chapter 2 - State of the art: A literature review of the concepts for a better understanding of the work performed.
- Chapter 3 - Methodology: The materials, techniques and methods used in the analysis of the samples are outlined.
- Chapter 4 - Results and discussion: The results obtained are presented and discussed.
- Chapter 5 - Conclusions and future work.

Chapter 2

State of the Art

2.1 Additive manufacturing

2.1.1 Introduction to additive manufacturing

Additive Manufacturing (AM) has been defined by the ISO/ASTM 52900 committee as: "process of joining materials to make parts from 3D model data, usually layer upon layer, as opposed to subtractive manufacturing and formative manufacturing methodologies" [1].

Additive manufacturing techniques have been developed from Rapid Prototyping (RP) techniques, that were introduced in the late 1980s, early 1990s as a solution for faster product development, due to the ability to produce complex shaped prototypes in small intervals of time to the production of end-use products.

An AM process starts with a 3D CAD design model of what we pretend the part to be. This model is then decomposed into thin slices. The information is sent to the AM machine which builds the product layer by layer.

Opposing to the traditional subtractive manufacturing processes, such as machining operations that produce the parts by removing the material from a larger piece, the AM processes create 3D components by adding layers of material onto each other. This allows for a higher degree of designing freedom and the potential to create complex shapes and geometries. These, together with the rapid prototyping are the great advantages of AM - Fig 2.1. AM has been applied in the fields of aerospace, bio-engineering, automotive and product development [2, 3].

From an environmental stand point not enough information is known as to ascertain the impact of AM on the environment. Most of the information related to AM is still a maybe - Fig 2.2.

At the moment, in the AM processes, due to the small dimensions of the building chambers only small parts are being produced, this results on a limited area of possible applications. Because the AM processes is still being studied and developed in controlled environments, mainly laboratories and research centres, is difficult to make considerations about its impact on the environment and on the economy [3].

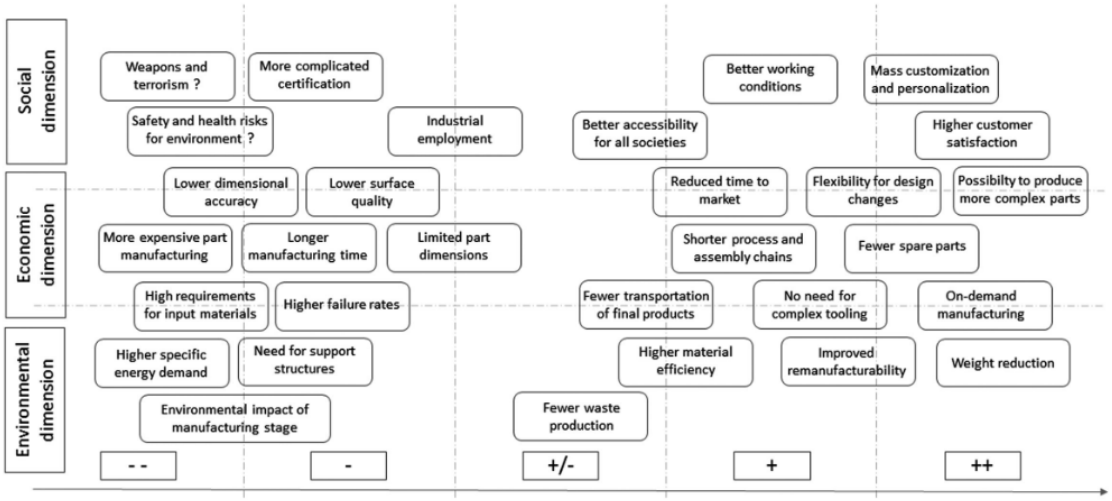

Figure 2.1: Benefits (++) and weaknesses (−−) of additive manufacturing processes compared to traditional manufacturing processes [3]

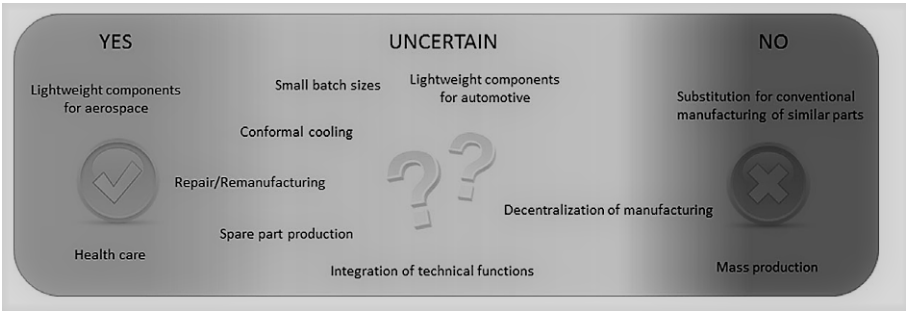

Figure 2.2: Potential benefits of AM application fields from an environmental perspective [3].

2.1.2 Additive manufacturing processes

There are seven different processes of Additive Manufacturing defined by the ISO/ASTM 52900 committee [1]:

1. **Material extrusion** - AM process in which material is selectively dispensed through a nozzle or orifice.
2. **Material jetting** - AM process in which droplets of build material are selectively deposited.
3. **Binder jetting** - AM process in which a liquid bonding agent is selectively deposited to join powder materials.
4. **Sheet lamination**- AM process in which sheets of material are bonded to form an object.
5. **Vat photo-polymerisation** - AM process in which liquid photo-polymer in a vat is selectively cured by light-activated polymerisation
6. **Powder bed fusion** - AM process in which thermal energy selectively fuses regions of a powder bed.
7. **Directed energy deposition**- AM process in which focused thermal energy is used to fuse materials by melting as the material is deposited.

2.1.3 Metal additive manufacturing

The additive manufacturing of metals is referred as: metal additive manufacturing (MAM) and is a fast-developing technology, mainly because it has lost its purpose of being only used to obtain prototypes and is currently seen as a manufacturing technology [2, 4].

As mentioned previously, the advantages of AM are its rapid prototyping and the development of more complex structures. It has also been used in the modification of finished products, by fixing or further developing them. However, it is still blocked by low productivity, poor surface quality and uncertainty of the final mechanical properties [5].

From the seven processes mentioned in 2.1.2, there are four processes that can use metallic materials:

1. **Powder Bed Fusion** – Selective Laser Sintering (SLS), Selective Laser Melting (SLM), Electron Beam Melting (EBM) and Direct Metal Laser Sintering (DMLS);
2. **Directed Energy Deposition** - Electron Beam Additive Manufacturing (EBAM) and Laser Engineered Net Shaping (LENS);
3. **Binder Jetting**
4. **Sheet Lamination** or Laminated Object Manufacturing (LOM)

This work will be focused on the Powder Bed Fusion technique of Selective Laser Melting.

2.2 Selective Laser Melting

Selective Laser Melting is an additive manufacturing technique that was developed at the Fraunhofer Institute ILT (Institute for Laser Technology) in Aachen Germany in 1995, in which a high-power density laser is used to melt the metallic powder layer by layer [6].

As other AM processes, SLM has several advantages when compared to traditional machining like near-net-shape fabrication with minimal or no post-processing, shorter lead-time, added functionality and more complex structures. This allows to have a wide range of application fields: aerospace, automobile, oil refinery, marine, construction, food, and jewellery industries, etc. Nevertheless, there are still problems in SLM mainly the low surface quality and even though the process can achieve almost fully dense (98-99%) parts, the remaining residual porosity may still be problematic to applications where high strength and fatigue resistance are required [7, 8].

2.2.1 SLM process

A schematic of the Selective Laser Melting process can be seen on Fig 2.3.

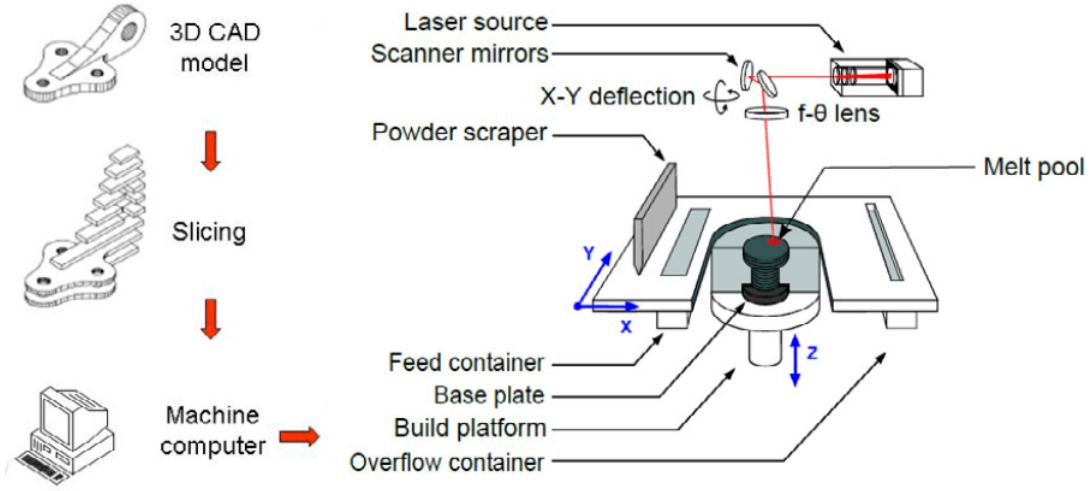

Figure 2.3: Selective Laser Melting process, [4]

The SLM process steps are based on [9]:

1. A 3D CAD design that is converted to a 2D slices and the setting of the process parameters
2. The feed containers are filled with the powder and the base plate is positioned in the build platform
3. The build platform is lowered, and a new powder layer is deposited
4. The high-density laser scans through the powder bed melting on the predefined path. After, the melt cools down and solidifies
5. The steps 3 and 4 are repeated until the component is finished
6. When it is finished, the base plate is removed from the build platform and the component is extracted. The unused powder is sieved before being used to create another component.
7. Parts may be heat treated to stabilise certain material phases, induce precipitation, or eliminate residual thermal stresses. The surface is finished by sand blasting or polishing. Additional machining, like threading or drilling, may also be performed to meet specific part requirements.

2.2.2 Process parameters

The process parameters involved in the SLM technique can be divide into four categories [4]:

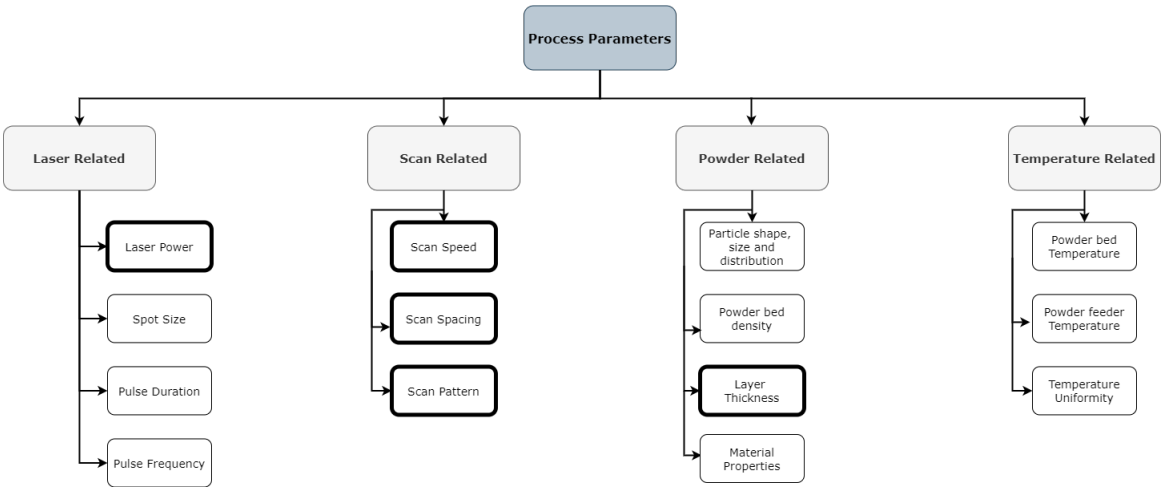

Figure 2.4: The most influential process parameters that affect the quality of a part processed by SLM [4]

The process parameters that have a higher influence on the optimisation of the SLM process, are represented in Fig 2.5 with the exception of the scanning pattern.

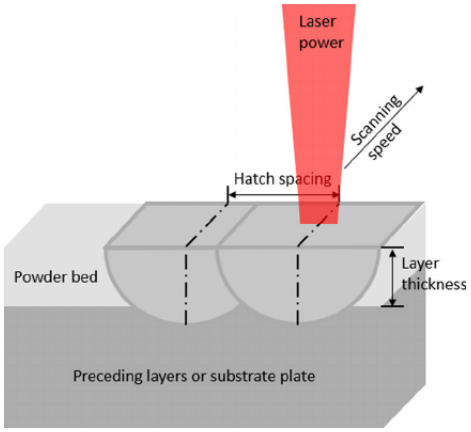

Figure 2.5: SLM process parameters: laser power, scanning speed, hatch/scan spacing, and layer thickness [10].

Laser power

Laser power is the applied energy per time unit of the laser beam. The range of laser power values goes from 20 W to 1 kW.
The required laser power depends on the melting point of the material and the powder bed temperature. The laser ray hits the powder heating it, the heat will be accumulated during the process increasing the powder bed temperature. It also depends on the absorptivity characteristics of the powder bed, which is influenced by material type and powder shape, size and packing density [11]. In Fig 2.6 are exemplified the effects of a partially penetrated

layer versus a satisfactory laser penetration.

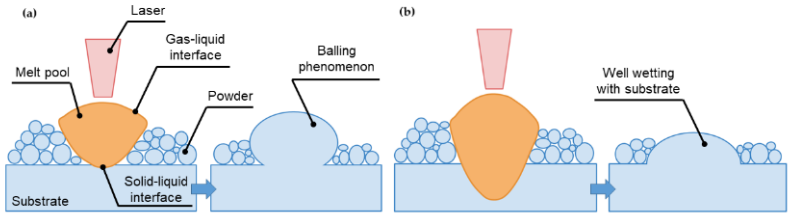

Figure 2.6: Solidification phenomenon during SLM: (a) partially penetration of laser into powder bed, (b) adequate laser penetration into powder layer [2]

Layer tickness

The layer thickness corresponds to the downward step of the build plate when depositing a new layer. It determines the volume of material that needs to be melted to consolidate a new layer of powder and hence the total amount of energy that is needed. During SLM, successive layers of powder are melted on top of each other, to ensure good connectivity between the layers, part of the previously fabricated layer needs to be remelted [9].

Scanning speed

Scanning speed is defined as being the speed at which the laser beam is moved across the powder bed. It controls the production time of the SLM process [9].

Scan/Hatch spacing

The scan/hatch Spacing is the distance between two adjacent scan vectors and determines the overlap between neighbouring melted pool tracks. A poor hatch spacing often results in regular porosity inbuilt parts as adjacent melt lines do not fuse completely [9, 10]. The effects of a poor hatch spacing can be seen in Fig 2.7.

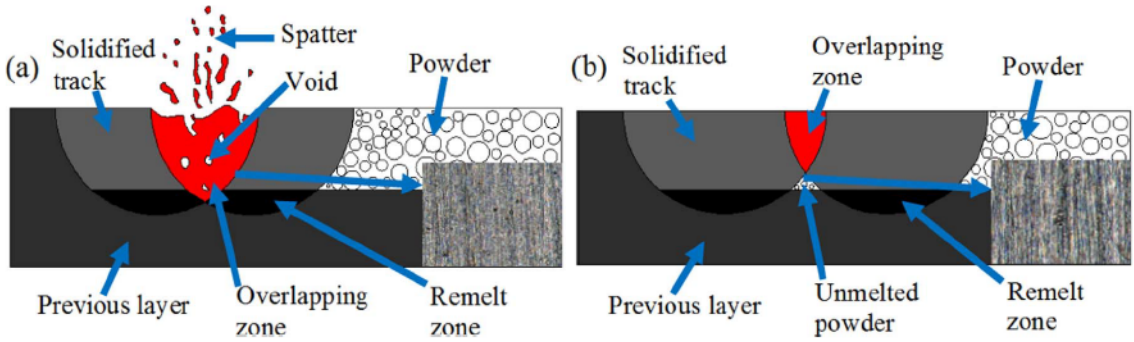

Figure 2.7: Effect schematic of scanning space/hatch on forming parts: (a) is too small; (b) is too large [8].

Scanning pattern

The scan pattern specifies the laser path within a layer. The most commonly used are the unidirectional and the bi-directional, represented in Fig 2.8, and the checkerboard pattern of alternating unidirectional fills in Fig 2.9. The scan strategy determines the difference in the scan patterns between layers. Patterns and strategies influence features such as porosity, microstructure, surface roughness and heat build-up in the finished metal components [4, 12, 13].

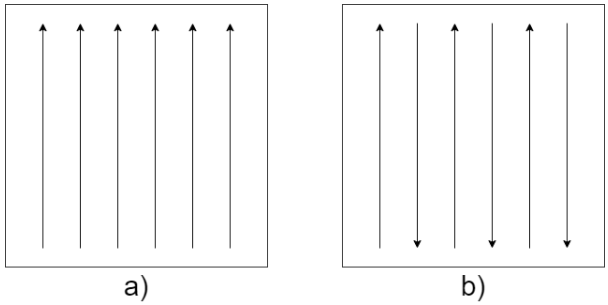

Figure 2.8: Scan Patterns: a) Unidirectional and b) Bi-directional. Adapted from [4].

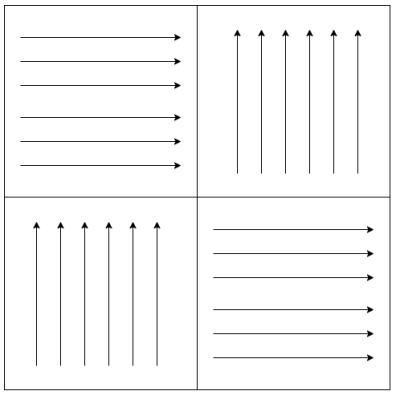

Figure 2.9: Scan pattern checkerboard. Adapted from [4].

2.2.3 Shortcomings of SLM

As previously mentioned, there are still problems in SLM mostly due to the physical complexity of the process.

The low surface quality and remaining residual porosity are still a serious concern when using SLM parts in applications where high strength and fatigue resistance are required. Cracking and spatter also negatively influence the SLM produced parts, hindering the expansion and use of the SLM process. An effect that results from the non-optimal SLM process parameters is the Balling Effect. This effect can result in the breaking up of the melted pool during SLM and produce particles with spherical shape [14] - Fig 2.6.

Porosity

The most common defect in SLM built parts is porosity. This is a consequence of the material's low laser absorptivity in the SLM wave-length resulting in the appearance of pores.

There are two types of pores: metallurgic and keyhole. The metallurgic pores also referred as hydrogen porosity are spherically shaped and have a small size, less than $100\mu m$. They originate from the gases trapped in the melt pool or evolved from the powder during merging. The keyhole pores are irregular shaped and large, bigger than $100\mu m$. They are caused by the fast solidification of the melted layer without the holes being fully filled. Keyhole pores are unlikely to be find in full penetration welds [4, 15, 16].

The influence of the scan speed on the porosity is represented in Fig 2.10. We can observe that slow scan speeds result in more metallurgic pores while faster scan speeds result in more keyhole pores.

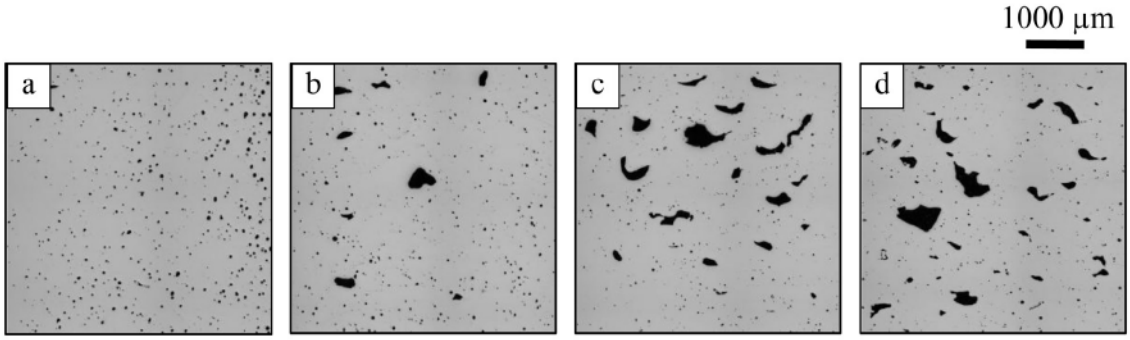

Figure 2.10: The influence of the scan speed on the porosity: a) 250 mm/s, b) 500 mm/s, c) 750 mm/s, and d) 1000 mm/s [15].

Lack-of-fusion defects

The quality of the SLM produced part is directly related to the cohesion of the melted powder. When the overlap between scan tracks and layers is not achieved lack-of-fusion (LOF) defects appear. There are two types of LOF defects: poor bonding defects and unmelted metal powders within the produced part - Fig 2.11. These are a consequence of the low energy input during the SLM process. A low laser power, a very thick layer, a fast scan speed or a wide scan spacing may be the root of the problem [17].

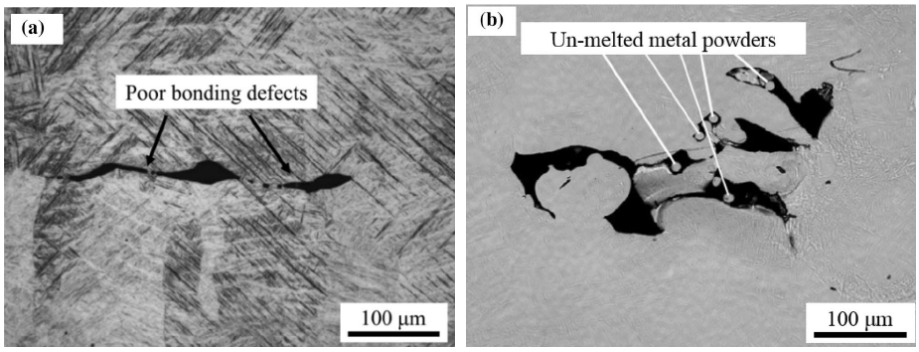

Figure 2.11: Lack-of-fusion defects: a) Poor bonding defects, b) Unmelted powders [17].

Cracks

In SLM the cracks are a consequence of the thermal variation experienced by the material during the process. Due to the cooling and heating cycles that occur during SLM a temperature gradient is created, consequently, the parts being built are put through this gradient which results in cracking [4].

Spatter and voids

When the power of the laser is higher than the threshold value, vaporization and spatter usually occur. As a consequence, there is not enough melted powder to fill in the space where the previous unmelted powder rested, resulting in voids. The spatter causes intrusions on the previous melted tracks, or on the still to melt powder. The uniformity and cohesion of the melted track is influenced and is considered a defect when the intrusions land on the part being built and it is seen as a contaminator when it does not remelt when rescanned [4, 8].

2.3 Maraging steel - AISI 18Ni300

Maraging steels are known for having good mechanical properties as high strength, high toughness, good weldability and dimensional stability. They are used in the aircraft and aerospace industry in which superior mechanical properties and weldability are the most important features, and in tooling and die-making industry, which requires superior machinability [18, 19, 20].

Maraging steels are different from conventional steels in that the main alloy component is nickel and have small quantities of cobalt, molybdenum, titanium and very small carbon content. They get their mechanical properties from a martensitic matrix that contains a high number density of nanometre-sized intermetallic precipitates [18, 20].

The term "Maraging" comes from the combination of "martensite" - the transformation of the face centred cubic high-temperature austenite phase of such alloys into martensite - and "aging" - subsequent age hardening treatment [21].

2.3.1 Strengthening mechanisms

These ultra-low carbon alloys have very high strength and hardness properties derived from precipitation of intermetallic compounds rather than carbon content. Nickel is the main alloying element, so, the overall contribution to strengthening is provided by the extremely tough Fe-Ni martensite. The aging of this martensite, containing, cobalt, molybdenum, and titanium as secondary intermetallic alloying metals in a supersaturated solid solution, provides additional strengthening by precipitation of nanosized intermetallic particles in the martensitic matrix [22].

2.3.2 Maraging steel in AM

The weldability, high strength and high toughness of the maraging steels are some of the reasons why this material can be used in additive manufacturing processes. When applied to

maraging steels, SLM could enable efficient manufacturing of an extensive variety of high-performance moulds and dies for pressing or forging complex-shaped metal products [18, 23].

2.4 Stainless steel - AISI 316L

The austenitic stainless steels are alloys of Fe-Cr-Ni with 16% to 25% of Cr and 7% to 20% of Ni. The reason why they are named austenitic is because their crystalline structure remains CFC at room temperature. It is due to its crystalline structure that the steels have such a high deformation ability. The reason that they have a higher corrosion resistance than the ferritic steels is that the carbides can be retained in a solid solution through rapid cooling to elevated temperatures [24].

The austenitic structure of stainless steel 316L gives excellent toughness, even at cryogenic temperatures. It has high corrosion resistance, and it is also a weldable material, but they are hard to machine [25].

SLM processed stainless steel 316L has been used in various industrial applications as: plastic injection and pressure die-casting moulds, extrusion dies, surgical tools, cutlery and kitchenware, maritime components, spindles and screws and general engineering [26].

2.5 Residual Stresses

Residual stress refers to the stresses that remain in an object even though no external forces are being applied. Residual Stresses can appear when the object is stressed beyond its elastic limit, resulting in plastic deformation. There are three main reasons for these stresses to arise [27]:

1. **Thermal Variations:** The cooling rate is not the same throughout the object. The surface cools much quicker, and as the inside of the object attempts to cool down, it is constrained by the exterior material, which causes residual stresses.

2. **Phase Transformations:** Due to the difference in volume that occurs between the newly formed phase and its neighbouring materials, an expansion or contraction of the material occurs, which causes residual stresses.

3. **Mechanical Processing:** When plastic deformation occurs in a non-uniform way through the cross-section of the material undergoing a mechanical manufacturing process.

Residual stresses can be classified in accordance with the deformation degree: macroscopic (Type I) or microscopic (Types II and III) [28] - Fig 2.12.

- **Type I** - The stress value is homogeneous across a large range of the component, to the scale of some tens of millimetres. These stresses lead to macroscopic dimensional variations of the component.

- **Type II** - These stresses are deviations to the average value of the Type I stress. The stress value is homogeneous across small areas of the component, like the material grains. These stresses come from the anisotropy of the crystal structures of the grains. They can result in dimensional variations on a macroscopic scale.

- **Type III** - These stresses are the deviations to the Type II stress. These stresses are inhomogeneous across the smallest material regions(several atomic distances), represent actions caused by crystalline defects and do not lead to deformation on a macroscopic scale.

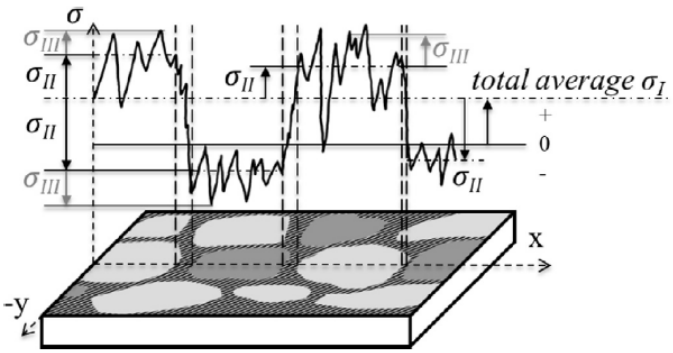

Figure 2.12: Definition of residual stresses (Type I, II, III) for a biphasic material [29].

2.5.1 Residual stresses in SLM

The residual stresses in SLM are caused by high temperature gradients and densification ratio and are influenced by the process parameters, resulting in form and dimensional deviations, stress-induced cracking and accelerated crack growth. A study made to show the influence of the scanning speed and the influence of the laser power in the residual stresses is presented in Fig 2.13.

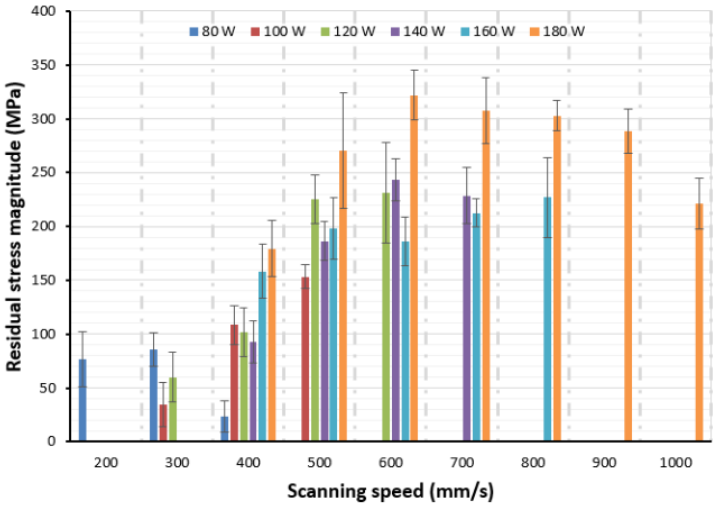

Figure 2.13: Variation of residual stress magnitude with laser power and scanning speed for Maraging Steel 300 [30].

In the SLM process, the thermal stresses occur from temperature gradients or from solidification induced shrinkage of neighbouring laser melted zones in solidified material. The thermal stresses can be described by two models, the temperature gradient mechanism (TGM) and

the cool-down mechanism [29].

In the TGM, the laser beam when melting the powder is transmitting energy to the material, causing it to expand thermally. However, this expansion is restricted by the colder surroundings and in the heat affected zone elastic compressive stresses are developed. Once there is no more energy being transmitted the cooling of the stretched areas causes them to contract and bend in the opposite direction. Tensile stresses are generated in the plastic deformed area Fig 2.14.

In the SLM process, the powder is locally melted and the transition to the liquid phase results in a metallurgical connection between the new track and the previously scanned layer. In the cool-down mechanism, the melted top layer is at a higher temperature than the underlying layer, therefore when the top layer cools down and solidifies, it contracts to a greater degree. However, due to the solid metallurgic connection between both layers this contraction is repressed. As a result tensile stress occurs on the top layer while compressive stress develops in the lower layer - Fig 2.15, [29].

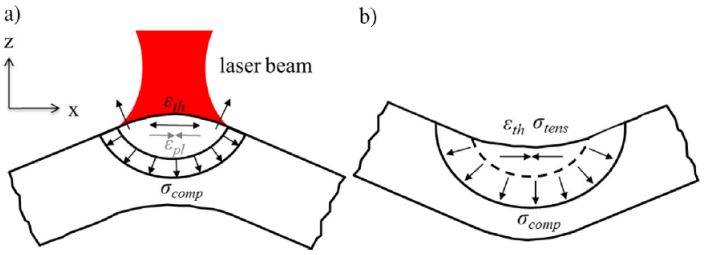

Figure 2.14: TGM inducing residual stresses: (a) when heating and (b) during cooling (plastic ε_{pl} and thermal elongation ε_{th}, tensile σ_{tens} and compressive σ_{comp} stress) [29].

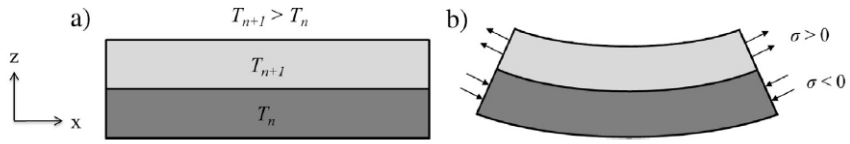

Figure 2.15: Cool-down phase inducing residual stress at solid layer connection (a) when heating, (b) during cooling [29].

Chapter 3

Materials and Methods

3.1 Materials

In this project the study of the residual stresses was made on samples produced by different materials, maraging steel 18Ni300 and stainless steel AISI 316L. The chemical composition of the powder given by the supplier is presented on Table 3.1 for the maraging steel samples and on Table 3.2 for the stainless steel samples. The SLM process parameters are presented in Table 3.3.

Table 3.1: Chemical Composition Limits of 18Ni-300 maraging steel [22].

Chemical Composition Limits											
Element	**C**	**Si**	**Mn**	**S**	**P**	**Co**	**Ni**	**Mo**	**Ti**	**Al**	**Fe**
Weight%	0.03 max	0.10 max	0.10 max	0.010 max	0.010 max	8.0-9.5	18.0-19.0	4.6-5.2	0.55-0.80	0.05-0.15	Bal

Table 3.2: Chemical Composition Limits of AiSi 316 L Stainless Steel [26].

Chemical Composition Limits											
Element	**C**	**Cr**	**N**	**Mn**	**Mo**	**Ni**	**P**	**S**	**Si**	**O**	**Fe**
Weight%	max 0.03	16–18	max 0.10	max 2.0	2.0–3.0	10–14	max 0.045	max 0.03	max 1.0	max 0.10	Bal

Table 3.3: SLM process parameters for the AISI 18Ni300 maraging steel and the AISI 316L stainless steel given by the supplier [22, 26].

	AISI 18Ni300	**AISI 316L**
Laser Power	400 W	300 W
Layer Thickness	40 μm	50 μm
Hatch Distance	95 μm	110 μm
Scan Speed	0.86 ms^{-1}	1.00 ms^{-1}
Particle size diameter	15 - 45 μm	15 - 45 μm

The samples made with AISI 18Ni300 maraging steel have a *"MAR"* designation while the samples made with AISI 316L stainless steel have a *"SS"* designation. The dimensions of the samples are indicated by the letter *"T"* for the bigger samples and the number *"0"* for the smaller samples. The samples and their nomenclature are presented in Fig 3.1 and the dimensions are on Table 3.4.

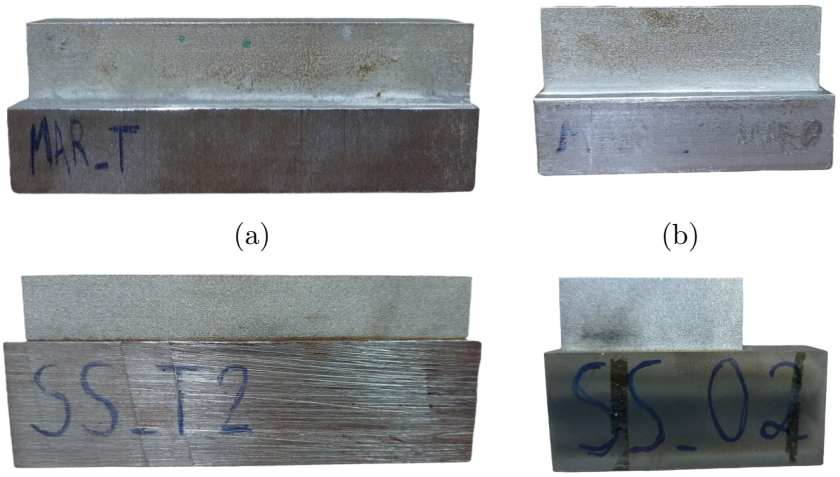

(a) (b)

(c) (d)

Figure 3.1: Samples: (a) MAR_T, (b) MAR_0, (c) SS_T2 and (d) SS_02.

Table 3.4: Sample dimensions.

Sample	**Length (mm)**	**Width (mm)**	**Height (mm)**
MAR_T	120	17	17
MAR_0	50	10	20
SS_T2	120	17	17
SS_02	50	10	20

The diffractometers used in this dissertation were a Seifert XRD 3000 PTS and a Proto iXRD, showed in Fig 3.2.

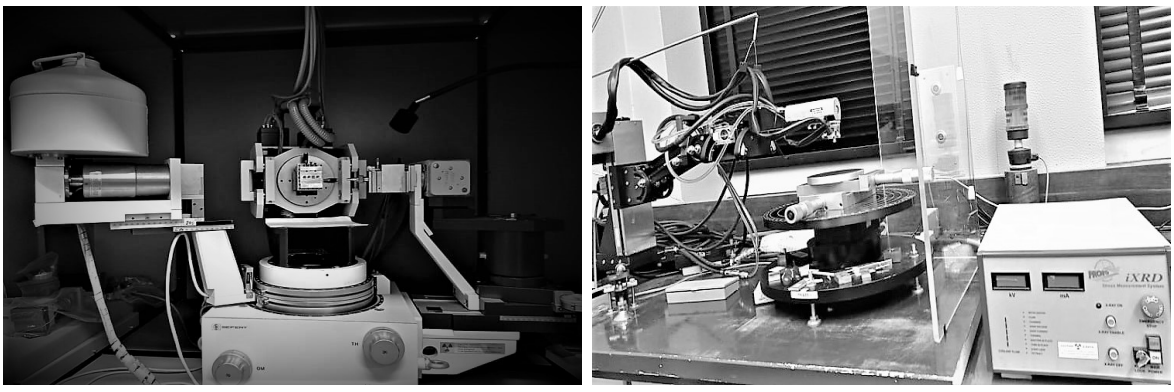

(a) (b)

Figure 3.2: X-Ray diffraction equipment's used: (a) Seifert XRD 3000 PTS and (b) Proto iXRD portable diffractometer.

3.2 Phase identification by X-Ray diffraction

In this dissertation, the X-Ray diffraction technique was used to identify the crystallographic phases, to quantify the amount of retained austenite and to determine the residual stresses distribution on the samples.

When radiation with wavelength, λ, of the same order of magnitude of the distance between atomic planes is scattered by the atoms of a crystalline structure, interference may occur. The condition for constructive interference is the Bragg's law:

$$2d_{hkl}\sin\theta = n\lambda \tag{3.1}$$

where d_{hkl} is the interplanar spacing of planes hkl, θ is the Bragg's angle, and n is the diffraction order (n=1,2,...).

Each crystalline material has an unique diffraction pattern. By comparing the obtained diffraction pattern with the ones in the data bases (JCPDS), an identification of the material is possible [28].

The diffractograms for all samples were obtained using a Seifert XRD 3000 PTS diffractometer, Fig 3.2a and the acquisition parameters are presented in Table 3.5.

Table 3.5: Acquisition parameters for phase identification.

Material	**Radiation**	**Collimator (mm)**	**Slit (mm)**	$\Delta 2\theta$ (°)	**Step (°)**	**Step time (s)**
AISI 18Ni300	Cu-Kα	2	1	30-150	0.05	4
AISI 316L	Cu-Kα	2	1	30-150	0.05	3

3.3 Quantification of austenite on maraging steel samples

The most accurate retained austenite measurement method is the X-ray diffraction. The direct comparison method was used, which relies on the fact that the diffracted peak intensities are proportional to the volume fraction of the corresponding phase, Eq 3.2. This method is essentially absolute and independent of external calibration. It can be used to determine low austenite contents (2%) with excellent precision.

$$I_{hkl} = \frac{KR_{hkl}V}{\mu} \tag{3.2}$$

where:

- I_{hkl} is the intensity of the diffracted peak (hkl);
- K is a constant related to the equipment and the experimental conditions;
- R_{hkl} is the theoretical intensity factor;
- V is the volume fraction of the phase;

- μ is the linear absorption coefficient;

For a biphasic material with volume fractions V_a and V_m:

$$V_a + V_m = 1 \tag{3.3}$$

$$I^a_{hkl} = \frac{K R^a_{hkl} V_a}{\mu} \tag{3.4}$$

$$I^m_{hkl} = \frac{K R^m_{hkl} V_m}{\mu} \tag{3.5}$$

Assuming the same experimental conditions for all measurements and calculating the ratio between peak intensities, both, the constant K and the linear absorption coefficient of the material, $\mu = V_a\ \mu_a + V_m\ \mu_m$ are eliminated:

$$\frac{V_a}{V_m} = \frac{I^a_{hkl} R^m_{hkl}}{I^m_{hkl} R^a_{hkl}} \tag{3.6}$$

Using Eq 3.3, the volume fraction of one the phase a:

$$V_a = \frac{\frac{I^a_{hkl}}{R^a_{hkl}}}{\frac{I^a_{hkl}}{R^a_{hkl}} + \frac{I^m_{hkl}}{R^m_{hkl}}} \tag{3.7}$$

This study was first made on a Seifert XRD 3000 PTS diffractometer with a Cu-Kα radiation, Table 3.6. The average penetration depth of this radiation on the material is of 1.5 μm.

Table 3.6: Acquisition parameters for the retained austenite quantification with Cu-Kα radiation used in the Seifert XRD 3000 PTS diffractometer, where A is Austenite and M is Martensite.

Peak	$\Delta\chi$ (°)	R_{hkl}	**Slit (mm)**	**Collimator (mm)**	$\Delta 2\theta$ (°)	**Step (°)**	**Step time (s)**
A (2 0 0)	0 - 40	81.6	2	2	48.5 - 53	0.01	2
M (2 0 0)	0 - 40	31.9	2	2	61.5 -68	0.02	4

Afterwards, to confirm the results obtained and dismiss if they are only relative to the surface of the samples, the same study was made with a Proto iXRD diffractometer, with Cr-Kα radiation, which has an average penetration depth of 5 μm in studied materials. The acquisition parameters are presented in Table 3.7.

Table 3.7: Acquisition parameters for the retained austenite quantification with Cr-Kα radiation used in the Proto iXRD diffractometer, where A is Austenite and M is Martensite.

Peak	β (°)	R_{hkl}	**Collimator (mm)**	2θ (°)	**Exposure Time (s)**
A (2 0 0)	37	29.9	2	79	100
M (2 0 0)	37	17.1	2	106	100
A (2 2 0)	26	44.1	2	128	100
M (2 1 1)	12	161.1	2	156	100

3.4 Residual stresses determination by X-ray diffraction

The principle of residual stress determination by X-ray diffraction lies in using the shift of the diffraction peak to obtained the strains, and through them calculate the stresses using the equations of continuum mechanics. For the X-ray diffraction the strains are determined from the variations of the interplanar distance of a family of crystalline planes (hkl), that relates to the peak position variation through Bragg's Law, Eq 3.1.

The elastic strains in the direction to the normal of the selected crystalline planes can be determined by calculating the strains, Eq 3.8, or differentiated the Bragg's Law, Eq 3.9:

$$\varepsilon = \frac{d - d_0}{d_0} = \frac{\sin\theta_0}{\sin\theta} - 1 \tag{3.8}$$

$$\varepsilon = -\frac{1}{2}\cot\theta_0 \Delta 2\theta \tag{3.9}$$

where d and d_0 are the interplanar distances of the material with and without stress, θ and θ_0 are the respective diffraction angles. The precision of the results increases for higher angles of diffraction - decrease of the cotangent therm.

For a material without stresses, the interplanar distance is independent of the plane's orientation in relation to the surface of the part. The orientation is defined by the Ψ angle, which is the angle that the normal to the planes makes with the normal of the surface of the part. If the material is being subject to a stress, the interplanar distance becomes a function of the Ψ angle. For this reason, the most adequate method for the determination of the residual stresses is the multiple exposures method, in which the crystallographic deformation for different values of the Ψ angle are measured.

Considering a homogeneous, isotropic and elastic solid, the relations between the stresses and the strains are obtained through the principles of continuum mechanics, Eq 3.10 [28]:

$$\varepsilon_{ij} = \frac{1+\nu}{E}\sigma_{ij} - \frac{\nu}{E}\sigma_{kk}\delta_{ij} \tag{3.10}$$

where:

- ε_{ij} is the components of the strain tensor
- σ_{ij} is the components of the stress tensor
- E is the Young's modulus

- ν is the Poisson's ratio of the material
- δ_{ij} is the Kronecker symbol

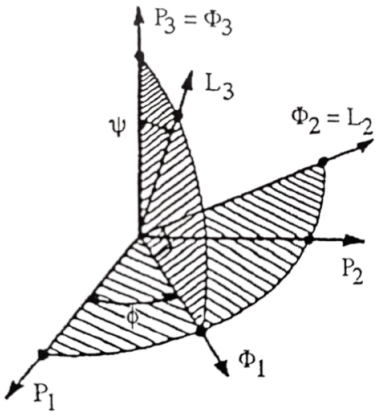

Figure 3.3: **L** is the laboratory referential, related to the diffraction conditions. **P** is the sample referential. σ_Φ is the stress direction of interest.

The measured strain is the projection of the $\varepsilon_{\phi\Psi}$ tensor onto the measurement direction, L_3, perpendicular to the crystalline planes and referenced on the coordinates system of the part by the angles Ψ and ϕ, Fig 3.3.

For a biaxial state of stress, the strains are related to the stresses by equation, Eq 3.11 [28]:

$$\varepsilon_{\phi\Psi} = \frac{1}{2} S_2 \sigma_\phi \sin^2 \Psi + S_1(\sigma_{11} + \sigma_{22}) \tag{3.11}$$

where σ_ϕ is the normal stress, in the Φ_1 direction of the surface specimen and $\frac{1}{2}S_2$ and S_1 are the X-ray elastic constants for the family of lattice planes hkl.

The equation for the "$\sin^2 \Psi$" method is Eq 3.11. The stress σ_ϕ can be determined by graphic representation of the strain, ε, as function of $\sin^2 \Psi$, for which a minimum of two diffraction peaks for different values of Ψ are needed, while keeping the Φ angle constant. The value of σ_ϕ is determined from the slope of the graphic, knowing the value of $\frac{1}{2}S_2$ for the selected diffraction peak.

The two X-ray elastic constants, S_1 and $\frac{1}{2}S_2$ depend of the diffraction angle and are defined in Eq 3.12:

$$\begin{cases} S_1 = \frac{-\nu_{hkl}}{E_{hkl}} \\ \frac{1}{2}S_2 = \frac{1+\nu_{hkl}}{E_{hkl}} \end{cases} \tag{3.12}$$

The elastic constants, ν_{hkl} and E_{hkl} are different from the elastic macroscopic constants ν and E due to crystalline anisotropy.

In this work, the residual stress analysis before and after the removal of the sample from the build plate was made on the Proto iXRD diffractometer using the $sin^2\Psi$ method for stress calculation. The values of the X-ray elastic constants were taken from the literature.

For most of the data, a collimator of 2 mm was used with the exception of the layer closer to the build plate, where a 1 mm collimator was then used, to limit the area of the part irradiated due to the shading caused by the build plate.

For the Maraging Steel 18Ni300 samples a Cr-Kα radiation (20 kV, 4 mA) was used for the Fe-α 211 family planes. The residual stresses were calculated using the X-ray elastic constants of $\frac{1}{2}S2 = 5.83 \times 10^{-6} MPa^{-1}$ and $S1 = -1.28 \times 10^{-6} MPa^{-1}$.

In the AISI 316L samples, the Fe-γ 311 family planes were determined using a MnKα radiation source (13 kV, 4 mA). The residual stresses were calculated using the X-ray elastic constants of $\frac{1}{2}S2 = 6.98 \times 10^{-6} MPa^{-1}$ and $S1 = -1.87 \times 10^{-6} MPa^{-1}$.

A representation of the referential used during the study of the samples is on Fig 3.4a and the nomenclature used for the samples surface is on Fig 3.4b. The acquisition parameters are presented in Table 3.8.

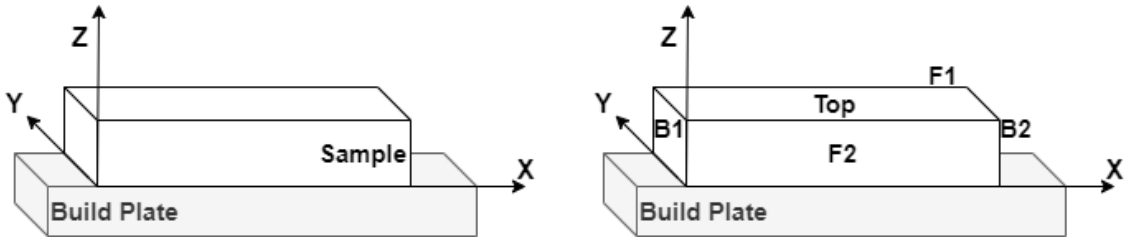

(a) (b)

Figure 3.4: (a) Schematic representation of the referential used during the study of the samples (b) Nomenclature of different samples surfaces.

Table 3.8: Acquisition parameters used for each material in residual stresses determination by X-ray diffraction with the Proto iXRD diffractometer.

Material	**Exposure Time (s)**
AISI 18Ni300	30
AISI 316L	20

Since the average penetration of the X-ray is about 5 μm on the analysed material, with the selected experimental conditions, the determined residual stresses are characteristic of the analysed surface. The analysis of the in-depth distribution of the residual stresses was performed after successive layer removal by electrolytic polishing, to avoid the reintroduction of further residual stresses. The electrolytic polishing was carried out using a Proto Electrolytic Polisher, model 8818, equipment - Fig 3.5a.

Successive layers were removed in a circular area of 10 mm of diameter, Fig 3.5b. The removal was made with a diluted solution of 50% Proto Electrolyte A with water for the AISI 316L stainless steel sample and with 100% Proto Electrolyte A for the AISI 18Ni300 maraging steel sample.

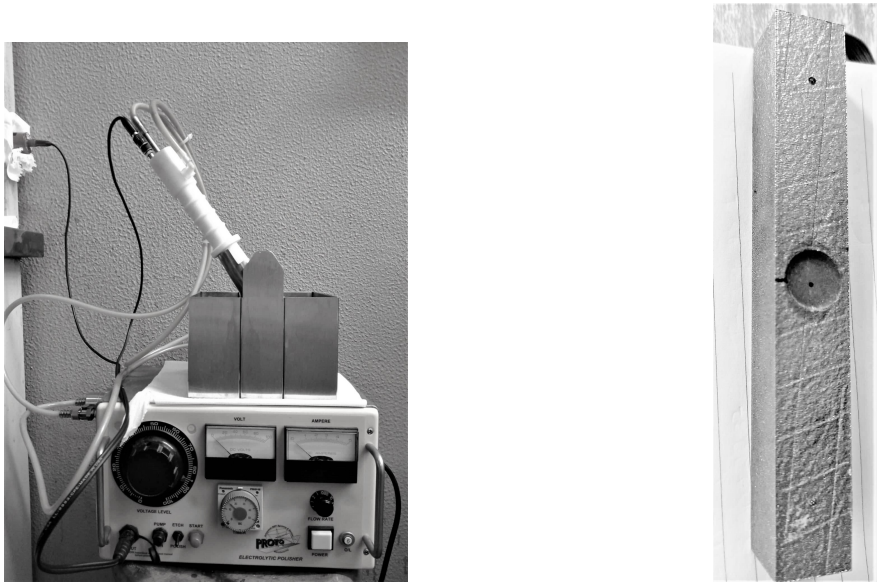

(a) (b)

Figure 3.5: (a) Proto Electrolytic Polisher, model 8818 and (b) The Top face of the SS_T2 sample after the electrolytic polishing method.

3.5 Residual stresses determination by Incremental hole drilling

The incremental hole drilling is a well established method to determine near surface in depth residual stress profiles in industry. This method involves incrementally drilling a small hole at the material surface, of typically 1 mm to 2 mm of diameter, up to a depth equal to the diameter and measuring the strain relief caused by the hole presence, using strain gauges. Before drilling, the strain gauges are placed on the surface around the hole location. Once the material is removed the stresses relax and the corresponding strains are measured. The measurement of the relieved strains, in three different directions, after each incremental depth steps yields enough information to calculate the plane stress states. From these, the corresponding principal stresses σ_{max} and σ_{min} and their orientation β can be found, [31].
The relation between the principal residual stresses and the relieved residual strains is given by the general equation Eq 3.13:

$$\varepsilon = (\sigma_{max} + \sigma_{min})\overline{A} + (\sigma_{max} - \sigma_{min})\overline{B}cos(2\beta) \tag{3.13}$$

Where $\overline{A}$ and $\overline{B}$ are the hole drilling calibration constants for the finite area strains. These must be determined previously by finite element analysis – see calibration coefficient tables from ASTM E 837 [32].

A tri-axial rosette measures the strain relief around the area of the hole, Fig 3.6a. This method is considered to be semi-destructive, due limited material removal that can be tolerated and/or repaired.

The original residual stresses present at the hole location are evaluated from the strains relieved by hole-drilling. In particular, for the non-uniform stress case, the surface strain relief measured after completing hole depth step j depends on the residual stresses that existed in

the material originally contained in all the hole depth steps $1 \leq k \leq j$, Eq 3.14, [32].

$$\varepsilon_j = \frac{1+\nu}{E} \sum_{k=1}^{j} \overline{a_{jk}} (\frac{\sigma_x + \sigma_y}{2})_k + \frac{1}{E} \sum_{k=1}^{j} \overline{b_{jk}} (\frac{\sigma_x - \sigma_y}{2})_k \cos 2\theta + \frac{1}{E} \sum_{k=1}^{j} \overline{b_{jk}} (\tau_{xy})_k \sin 2\theta \qquad (3.14)$$

where:

- j is the number of hole depth steps so far
- ε_j is the relieved strain measured after j hole depth steps
- $(\sigma_x)_k$ is the normal x-stress within hole depth step k have been drilled
- $(\sigma_y)_k$ is the normal y-stress within hole depth step k have been drilled
- $(\tau_{xy})_k$ is the shear xy-stress within hole depth step k have been drilled
- θ is the angle of the strain gage from the x-axis
- the calibration constants $\overline{a_{jk}}$ and $\overline{b_{jk}}$ indicate the relieved strains in a hole j steps deep, due to unit stresses within hole step k.

From the strains the related stresses are calculated. These were determined, from the experimental obtained strain relaxation depth curves, using a software developed in Python by the GTR group, which is based on the ASTM standard method for in-depth non uniform stress calculation in thick samples. Tikhonov regularisation is used to smooth the final residual stress profiles, as a way to mitigate the influence of the ill-condition numerical effect of the inverse problem involved [32].

The incremental hole drilling method is often linked to the XRD method, which provides reliable results at material's surface. However, due to the surface roughness a misplacement of the zero point could be the source of some inaccuracy in the assumed depth in the first increments.

In this work 6-blades inverted cone end mills with 1.6 mm was used to drill a hole, step by step, with increments varying between 0.025 mm and 0.05 mm, up to 1 mm total depth. Two types of strain gauge rosettes were used: ASTM type A (Vishay CEA-06-062UL-120) and type B (Vishay CEA-06-062UM-120). The equipment used was a Vishay RS 200 milling guide connected to a HBM Spider 8-30 DAQ system, Fig 3.6c. This equipment enables a drilling speed of around 400000 rpm.

The experimental conditions for each material are presented in Table 3.9. The nomenclature and schematic representation of the points used for the study using the incremental hole drilling method are presented in the Fig 3.7.

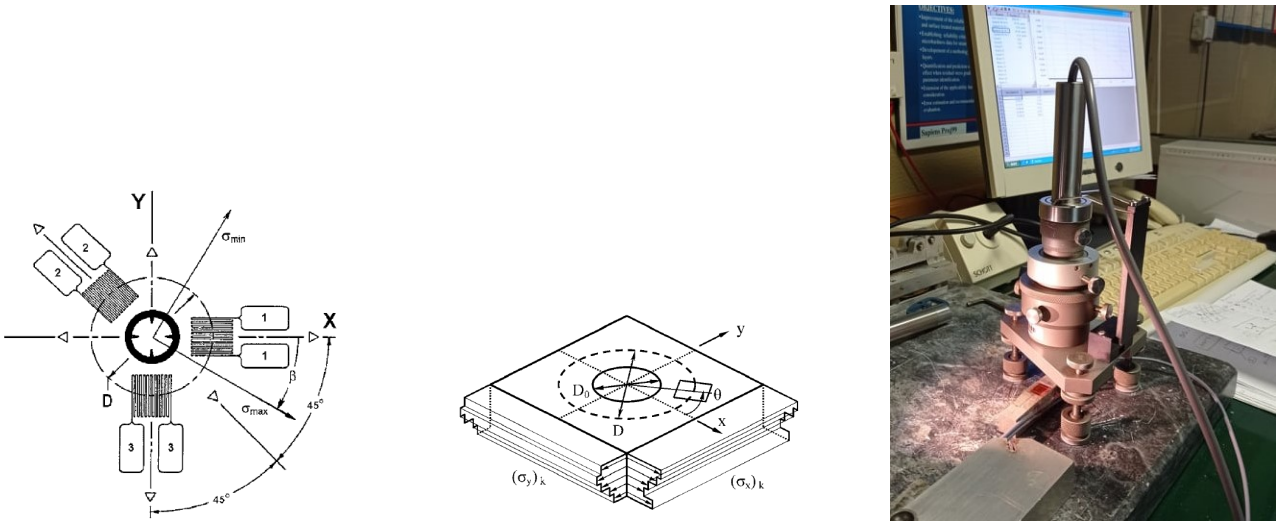

Figure 3.6: Incremental Hole Drilling: (a) Schematic Geometry of a Typical Three-Element Clockwise (CW) Hole-Drilling Rosette, (b) Hole Geometry and Residual Stresses for non-uniform stresses where D is the diameter of the gage circle and D_0 is the diameter of the drilled hole [32] and (c) Vishay RS 200 milling guide connected to a HBM Spider 8-30 DAQ system at the GTR lab.

Table 3.9: Mechanical properties of both materials and the rosettes used in the Incremental hole drilling.

Material	**Mechanical Properties**		**Rosettes**
	E **(GPa)**	ν	
AISI 18Ni300	190	0.3	CEA-06-062UL-120
AISI 316L	179	0.3	CEA-06-062UM-120

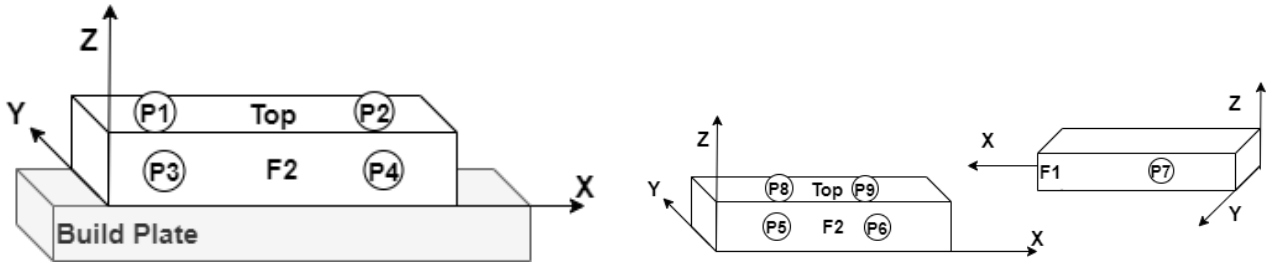

Figure 3.7: Schematic representation of holes drilled and their nomenclature (a) before the removal of the build plate and (b) after the removal of the build plate.

3.6 Metallographic analysis

3.6.1 Sample preparation

The schematic of the sectioning can be seen in Fig 3.8. The original sample was divided into three through two cross sectional cuts, afterwards, the most inside piece was cut in half perpendicularly to the previous cut. The planes XY and YZ were then available for analysis.

For the sectioning of the parts a Struers Labotom, was used - Fig 3.10a. The samples were encapsulated in hot epoxy using the Struers Prestopress equipment, Fig 3.10b. Subsequently, the samples were polished, Fig 3.9, using the Struers Planopol/Pedemax 2 (Fig 3.10c).

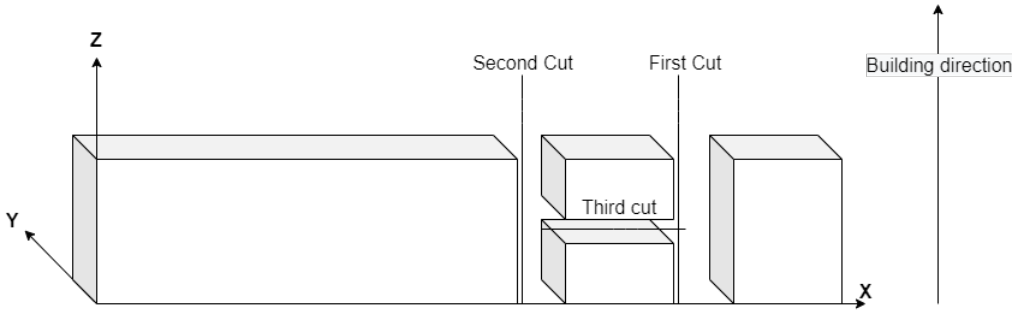

Figure 3.8: Schematic of the sectioning of the samples MAR_0 and SS_T2.

Surface	Abrasive/ Size	Load Lb. (N)/ Specimen	Base Speed (rpm)/Direction	Time (min:sec)
UltraPrep metal-bonded disc	45-µm diamond, water cooled	6 (27)	240-300 Comp.	Until Plane
ApexHercules H rigid grinding disc	9-µm MetaDi Supreme diamond suspension*	6 (27)	120-150 Comp.	5:00
TriDent cloth	3-µm MetaDi Supreme diamond suspension*	6 (27)	120-150 Comp.	3:00
MicroCloth, NanoCloth or ChemoMet cloths	MasterPrep 0.05-µm alumina suspension, or MasterMet colloidal silica	6 (27)	120-150 Contra	2:00

*Plus Metadi fluid extender desired
Comp. = Complementary (platen and specimen holder both rotate in the same direction)
Contra = Platen and specimen holder rotate in opposite directions

Figure 3.9: Four-Step polishing procedure used to polish samples [33].

(a) (b) (c)

Figure 3.10: Equipment used for the preparation of samples for the microstructural analysis: (a) Struers Labotom used for the sectioning of the samples (b) Struers Prestopress - 3 used for the capsuling of the samples (c) Struers Planopol/Pedemax 2 used to polish the samples.

3.7 Microhardness test

The Vickers microhardness test method consist of an indentation made on the surface sample by a square based diamond pyramid with an angle of 136° between opposite faces subjected to a cylindrical load, Fig 3.11a. The diagonals of the square indentation left on the sample after the removal of the load are measured and the Vickers microhardness, HV, is calculated using Eq 3.15, where F is the load value in gf and d is the arithmetic mean of the two diagonals, in μm, d_1 and d_2, [33, 34].

$$HV = 1.854\frac{F}{d^2} \tag{3.15}$$

For the evaluation of the homogeneity of the samples the microhardness was measured in different locations, spread through the surface sample and the average value for each section was determined. The test was performed with a Shimadzu Microhardness tester, type-M, Fig 3.11b.

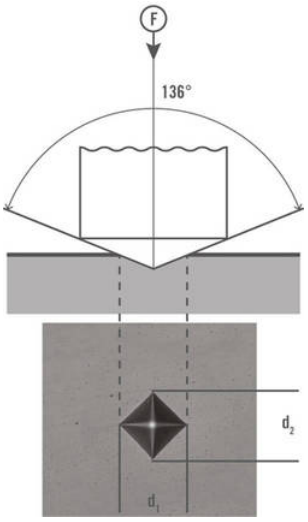

(a)

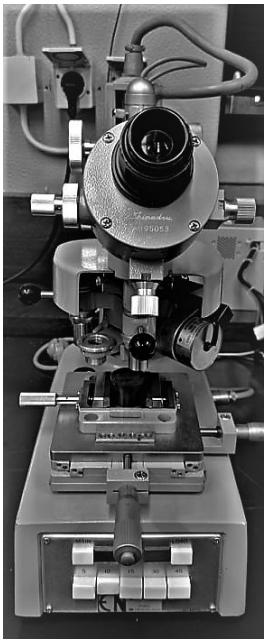

(b)

Figure 3.11: Vickers Microhardness method and equipment: (a) Schematic of the Vickers Microhardness method test, [35] (b) Shimadzu Microhardness tester, type-M, used for the Vickers Microhardness tests.

3.8 Optical microscopy

The microstructure was analysed by optical microscopy with a Nikon Optiphot metallographic microscope. For the ecthing of the AISI 316L stainless steel the sample surface was immersed during 7 minutes in Villela reagent. For the AISI 18Ni300 maraging steel, Nital 4% was used, immersing the sample surface during 2 minutes.

Chapter 4

Results and discussion

4.1 Phase identification

The study by XRD began with the analysis of the crystallographic phases present in the samples. This analysis is particularly important for the AISI 18Ni300 samples due to the possibility of containing retained austenite.

The diffractograms of the samples Mar_T and SS_T2, obtained with Cu-Kα radiation can be seen in Fig 4.1. Observing the Fig 4.1a corresponding to the AISI 18Ni300 samples the diffractogram shows the presence of martensite and retained austenite. The AISI 316L samples have only austenitic peaks, Fig 4.1b.

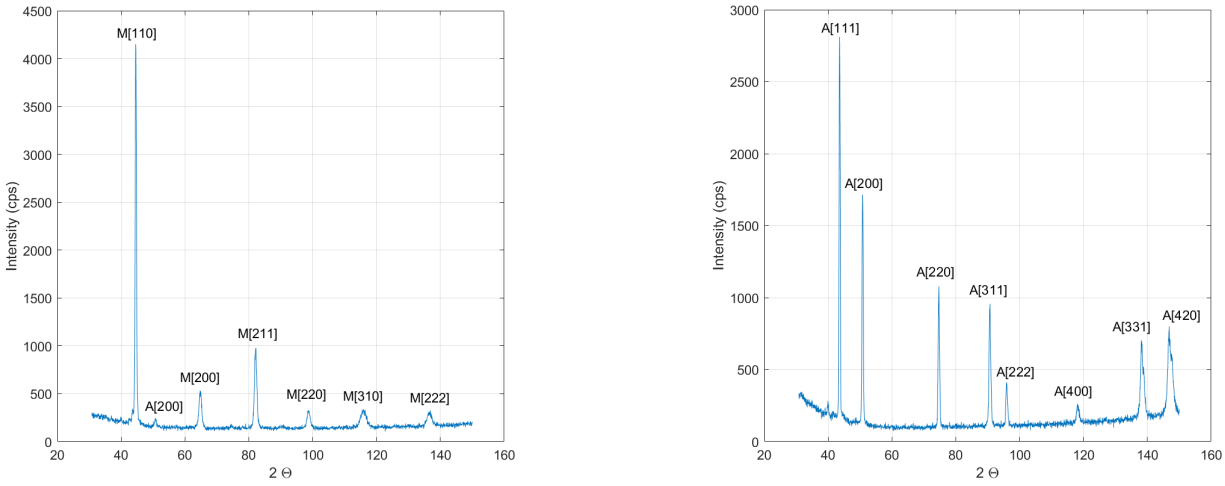

(a) (b)

Figure 4.1: Diffractograms: (a) AISI 18Ni300 and (b) AISI 316L.

4.2 Quantification of retained austenite in the Maraging Steel samples

Having been detected peaks of retained austenite in the diffractograms of the AISI 18Ni300 samples, a quantification of the retained austenite by XRD was made. To confirm the results obtained and dismiss if they are only relative to the surface of the samples, two radiations were used. The Table 4.1 shows the results obtained with Cu-Kα radiation and Table 4.2 the results with Cr-Kα radiation.

Table 4.1: Retained austenite percentage in the AISI 18Ni300 samples obtained with the Seifert diffractometer with Cu-Kα radiation.

Sample	**Face**	**Retained Austenite [vol%]**
MAR_T	Top	3 ± 2
	Frontal 1	4 ± 2
	Frontal 2	4 ± 2
MAR_0	Top	3 ± 1
	Frontal 1	6 ± 2
	Frontal 2	4 ± 2

Table 4.2: Retained austenite percentage in the AISI 18Ni300 samples obtained with the Proto diffractometer with Cr-Kα radiation.

Sample	**Face**	**Retained Austenite [vol%]**
MAR_T	Top	3 ± 1
	Frontal 1	6 ± 2
	Frontal 2	6 ± 1
MAR_0	Top	3 ± 1
	Frontal 1	6 ± 2
	Frontal 2	6 ± 2

Comparing the values in Table 4.1 and Table 4.2 the results are almost the same. The values of retained austenite in both samples are small and close to the resolution limit of the XRD technique (2%).

4.3 Metallographic analysis

The metallographic analysis was made with optical microscopy, as described in Section 3.8, in two sections of the samples: section XY, perpendicular to the building direction and section YZ, parallel to the building direction - Fig 4.2.

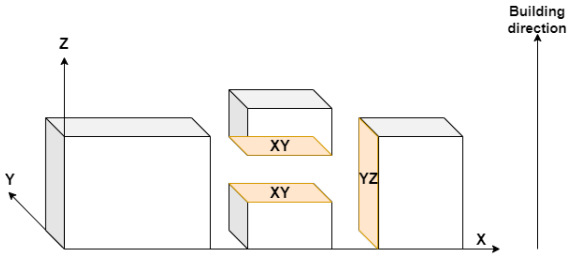

Figure 4.2: Schematic representation of the analysed sections.

The microstructure obtained in the cross section of the XY plane, perpendicular to the build direction is presented in Fig 4.3. The defined laser tracks and elongated grains result from the deposition, melting and cooling of the material, and allow for an idea of the scan strategy [23, 36].

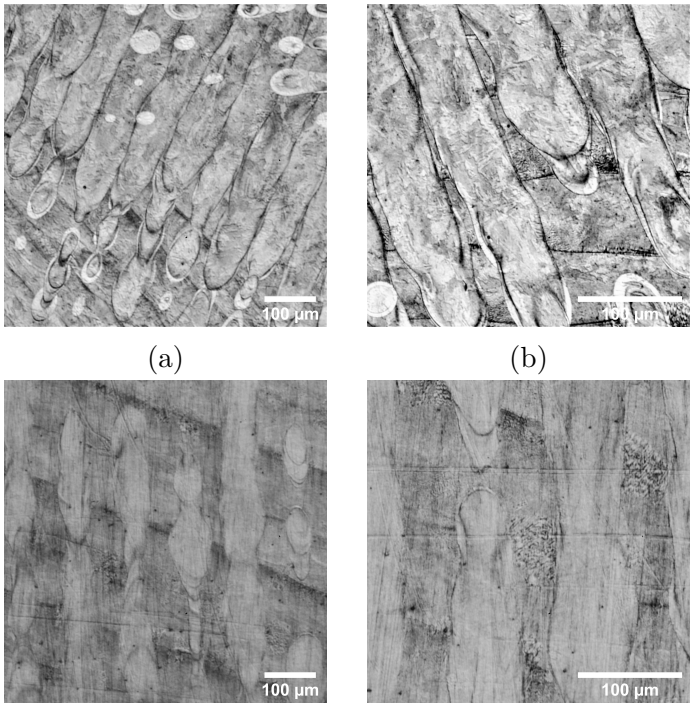

(a) (b)

(c) (d)

Figure 4.3: Microstructure obtained through optical microscopy on the XY cross section: (a) and (b) AISI 18Ni300 maraging steel; (c) and (d) AISI 316L stainless steel.

The microstructure of SLM produced samples has, on the section parallel to the build direction, YZ, semi-circular structures that correspond to the locally melted and rapidly solidified regions that are exposed to the scanning laser, Fig 4.4. In Fig 4.4b it is also possible to observe the formation of martensitic needles identified by the white circles.

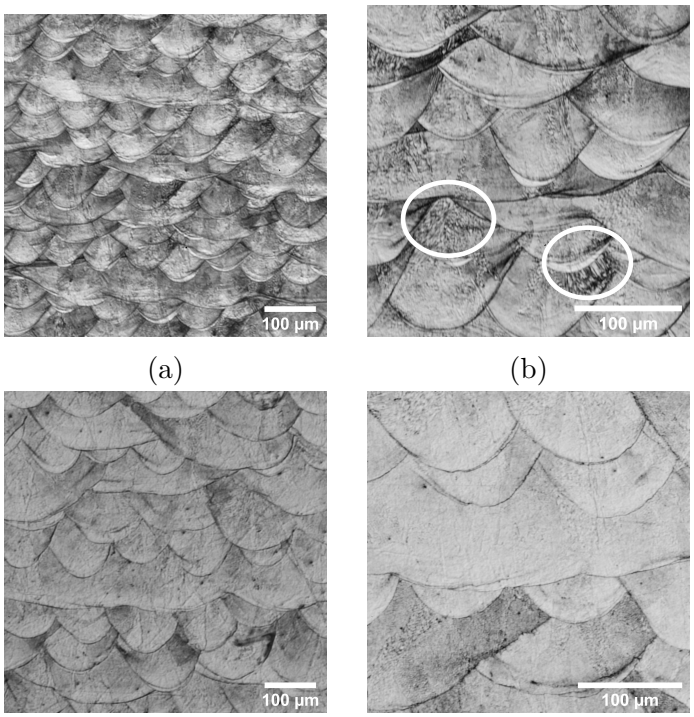

(a) (b)

(c) (d)

Figure 4.4: Microstructure obtained through optical microscopy on the YZ cross section: (a) and (b) AISI 18Ni300 maraging steel; (c) and (d) AISI 316L stainless steel. In (b) the circles identify the martensitic needles.

4.4 Microhardness test

The microhardness measurements were made in two sections: section XY, perpendicular to the build direction and section YZ, parallel to the build direction - Fig 4.2. The test parameters are in Table 4.3. Withing the sections the hardness was measured in different locations, spread through the plane. The results presented in Table 4.4 and Table 4.5 are the average values for each section. The results obtained are slightly higher than the ones from the supplier (200 HV for the AISI 316L and 360 HV for the AISI 18Ni300) [22, 26].

Table 4.3: Test parameters used for each material in the Vickers microhardness test.

Material	**Load (gf)**	**Time (s)**
AISI 18Ni300	25	5
AISI 316L	50	10

Table 4.4: Vickers microhardness test results for the AISI 316L sample.

	HV
Section XY	300 ±15
Section YZ	315 ±15

Table 4.5: Vickers microhardness test results for the AISI 18Ni300 sample.

	HV
Section XY	415 ±20
Section YZ	415 ±20

4.5 Residual Stresses

In the following sections, the results of the analysis on the residual stresses will be presented. This analysis was made with the build plate still connected to the samples, and after its removal by EDM (electric discharge machining). The aim is to check whether the removal of pieces from the boards, changes the residual stresses distribution. The analysis was performed by two different methods: the X-ray diffraction and the incremental hole drilling. This section ends with a comparison between the results obtained by the two methods.

Since the effect of the sample dimension did not affect the results, only the bigger samples will be discussed. The results obtained on the smaller samples can be seen in Appendixes A.1.2 and A.1.3.

4.5.1 Surface residual stresses on samples connected to the build plate

AISI 18Ni300, sample Mar_T

The residual stresses in the sample MAR_T while still attached to the build plate are showed in Fig 4.5.

The AISI 18Ni300 maraging steel sample presents tensile residual stresses in the top surface, Fig 4.5a and Fig 4.5b. For the remaining surfaces, the residual stresses are mostly compressive. In Fig 4.5d, σ_{zz} decreases in magnitude with the distance from the build plate. In the top surface, σ_{xx} and σ_{yy} have similar values. In the base surface, σ_{yy} and σ_{zz} decrease in magnitude when the distance from the build plate increases.

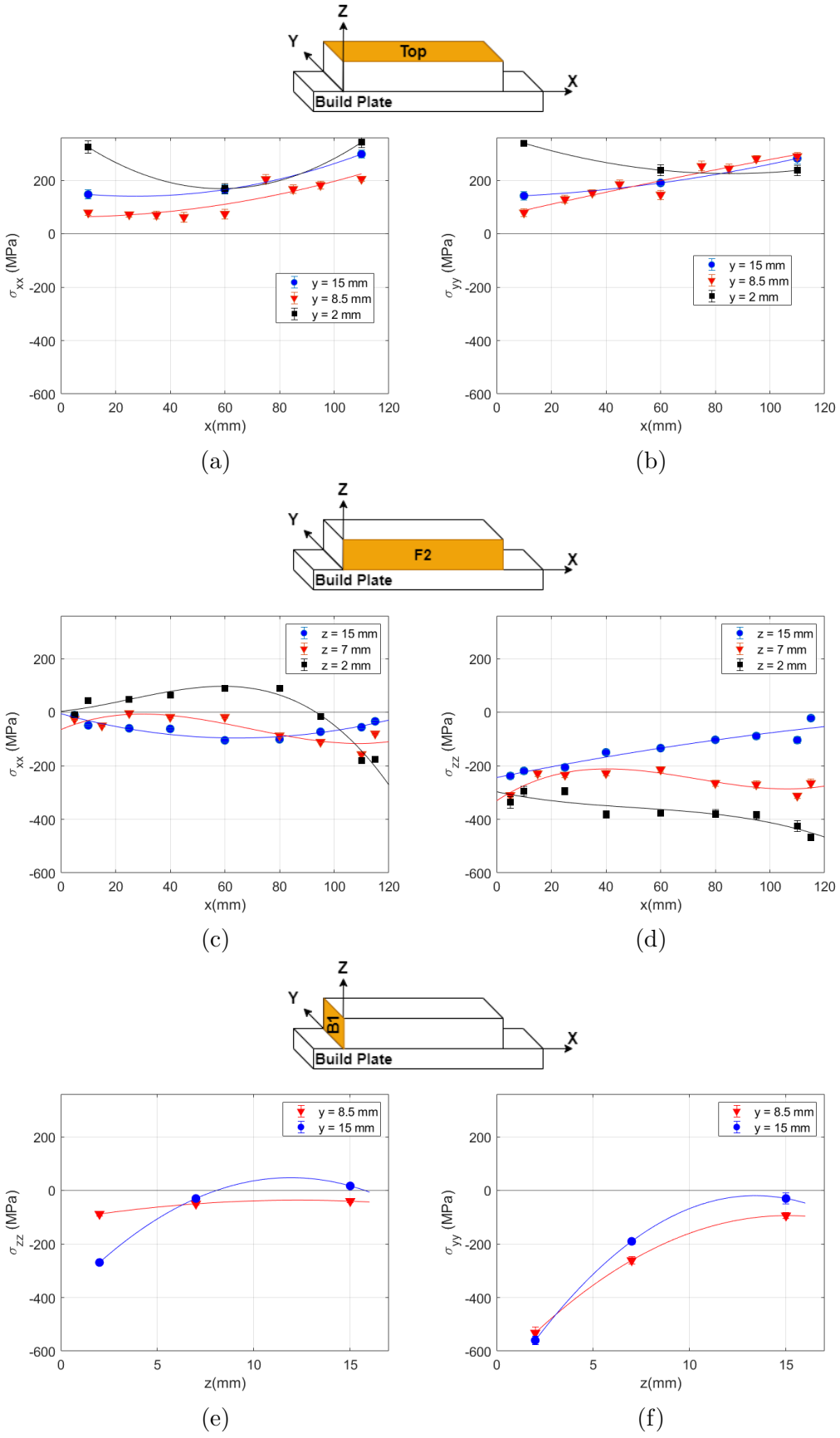

Figure 4.5: Residual stresses on the sample MAR_T while still connected to the build plate: (a) top surface σ_{xx} (b) top surface σ_{yy} (c) lateral surface σ_{xx} (d) lateral surface σ_{zz} (e) base surface σ_{zz} (f) base surface σ_{yy}

AISI 316L, sample SS_T2

The residual stresses of the sample SS_T2 before the removal of the build plate are showed in Fig 4.6.

The residual stresses in the AISI 316L stainless steel sample at the surface are mostly tensile. In the top surface, Fig 4.6a and Fig 4.6b, σ_{yy} has values of higher magnitude than σ_{xx}. This behaviour also occurs in the lateral surface, Fig 4.6c and Fig 4.6d, where σ_{zz} has values of higher magnitude than σ_{xx}. In the base surface, the σ_{zz} are tensile while, σ_{yy} has compressive residual stresses closest to the build plate.

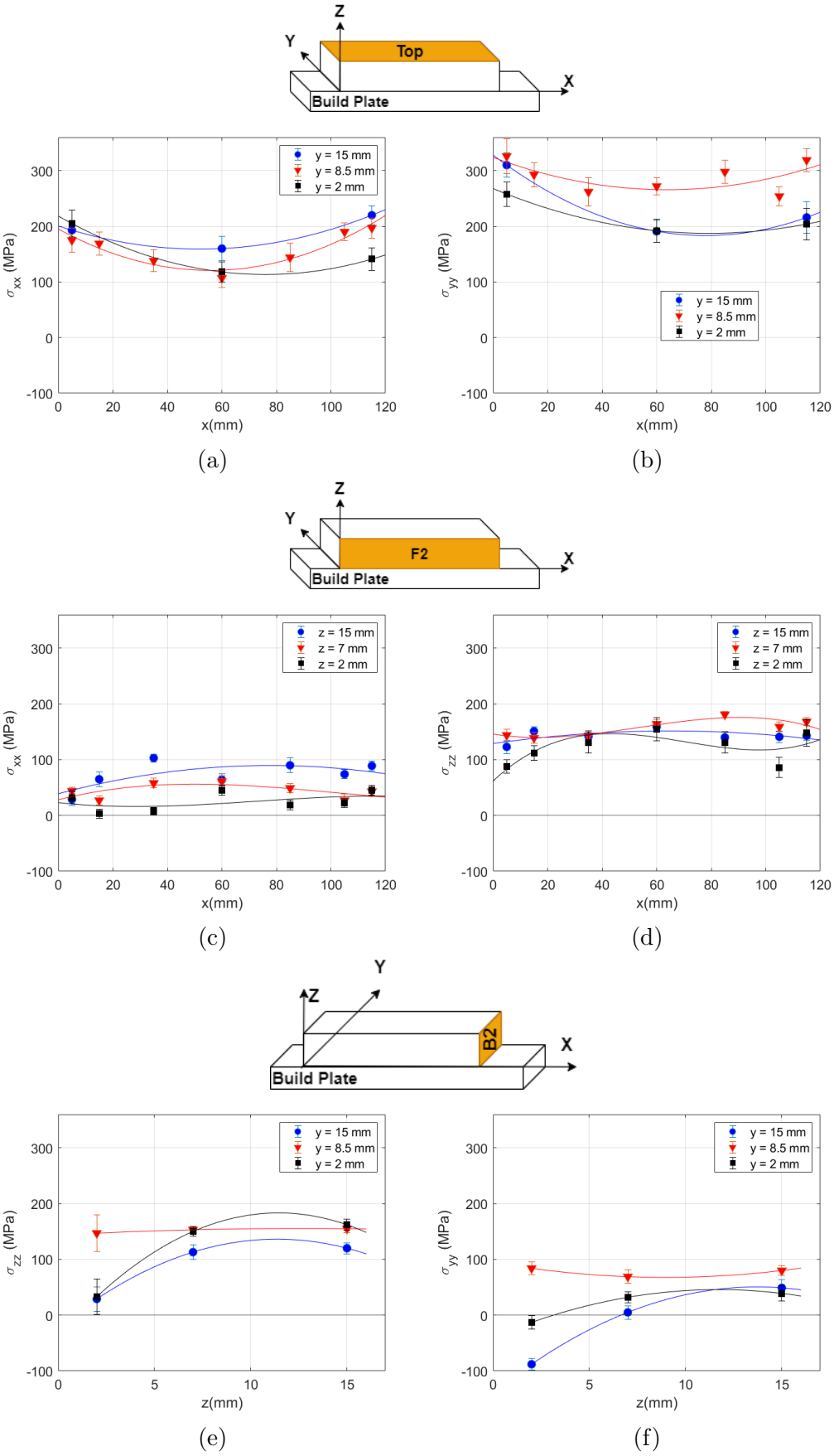

Figure 4.6: Residual stresses on the sample SS_T2 while still connected to the build plate: (a) top surface σ_{xx} (b) top surface σ_{yy} (c) lateral surface σ_{xx} (d) lateral surface σ_{zz} (e) base surface σ_{zz} (f) base surface σ_{yy}.

4.5.2 Surface residual stresses after sample removal from the build plate

AISI 18Ni300, sample Mar_T

The residual stresses in the sample MAR_T after the removal of the build plate are showed in Fig 4.7.

The residual stresses are tensile in the top surface and compressive in the other surfaces. The tendencies in Fig 4.5 and Fig 4.7 are very similar for each surface. It can be admitted that the removal of the build plate has little effect on the determined residual stresses.

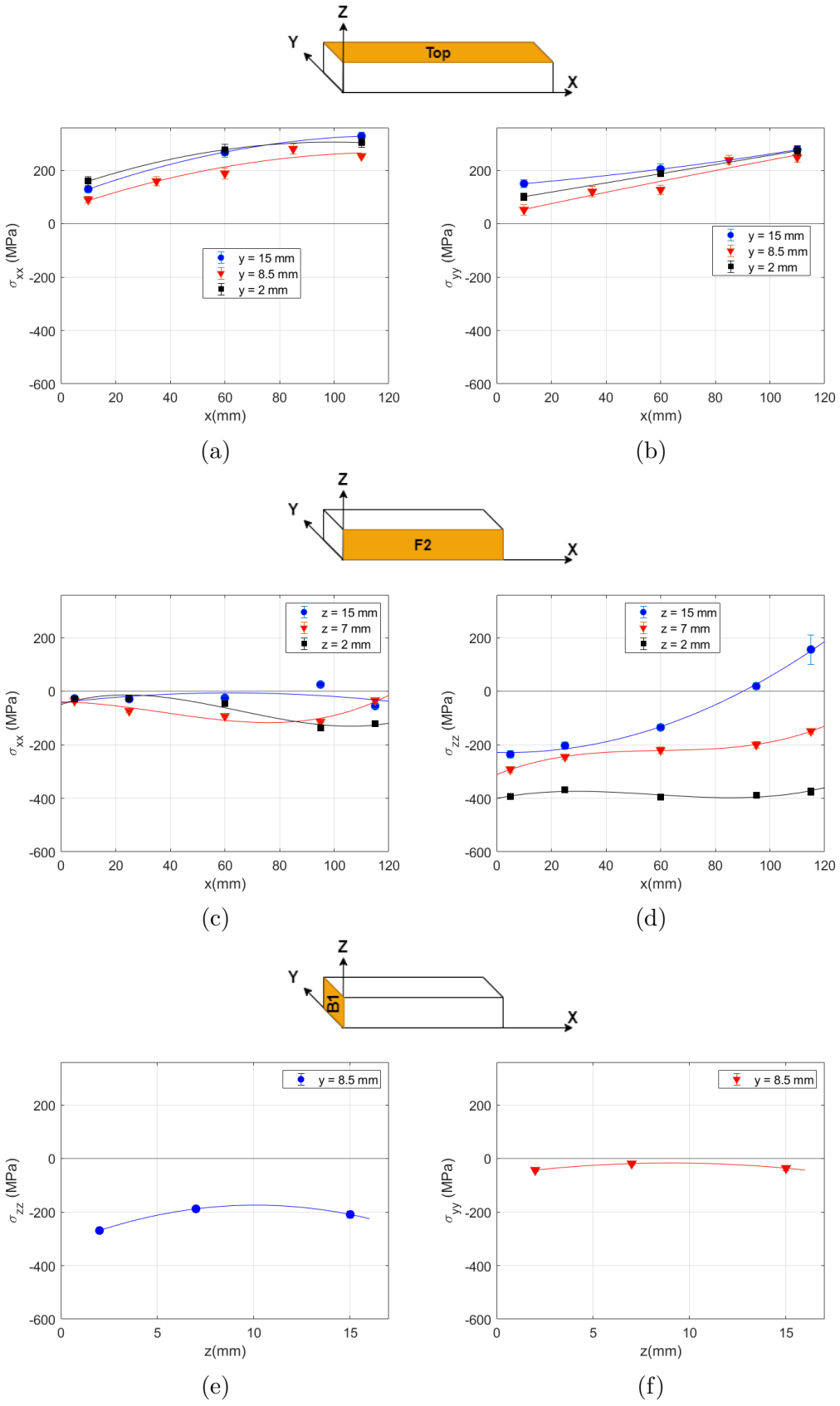

Figure 4.7: Residual stresses on the sample MAR_T without the build plate: (a) top surface σ_{xx} (b) top surface σ_{yy} (c) lateral surface σ_{xx} (d) lateral surface σ_{zz} (e) base surface σ_{zz} (f) base surface σ_{yy}.

AISI 316L, sample SS_T2

The Fig 4.8 shows the values of residual stresses determined for the sample SS_T2, after removal from the build plate.

The residual stresses are mostly tensile. The residual stresses, σ_{xx}, in both the top and lateral surfaces have lower values than the residual stresses σ_{yy} and σ_{zz} respectively.
The residual stresses for the AISI 316L samples before and after the removal of the build plate present very similar tendencies and close values.
Overall, for σ_{xx} in both the top and lateral surfaces there's a decrease in the centre of the surface, this is more noticeable in the top surface - Fig 4.6a and Fig 4.8a. In the lateral surface, for σ_{zz}, in the layers closest to the build plate (Fig 4.6d and Fig 4.8d) there's a decrease in the values of the residual stresses.

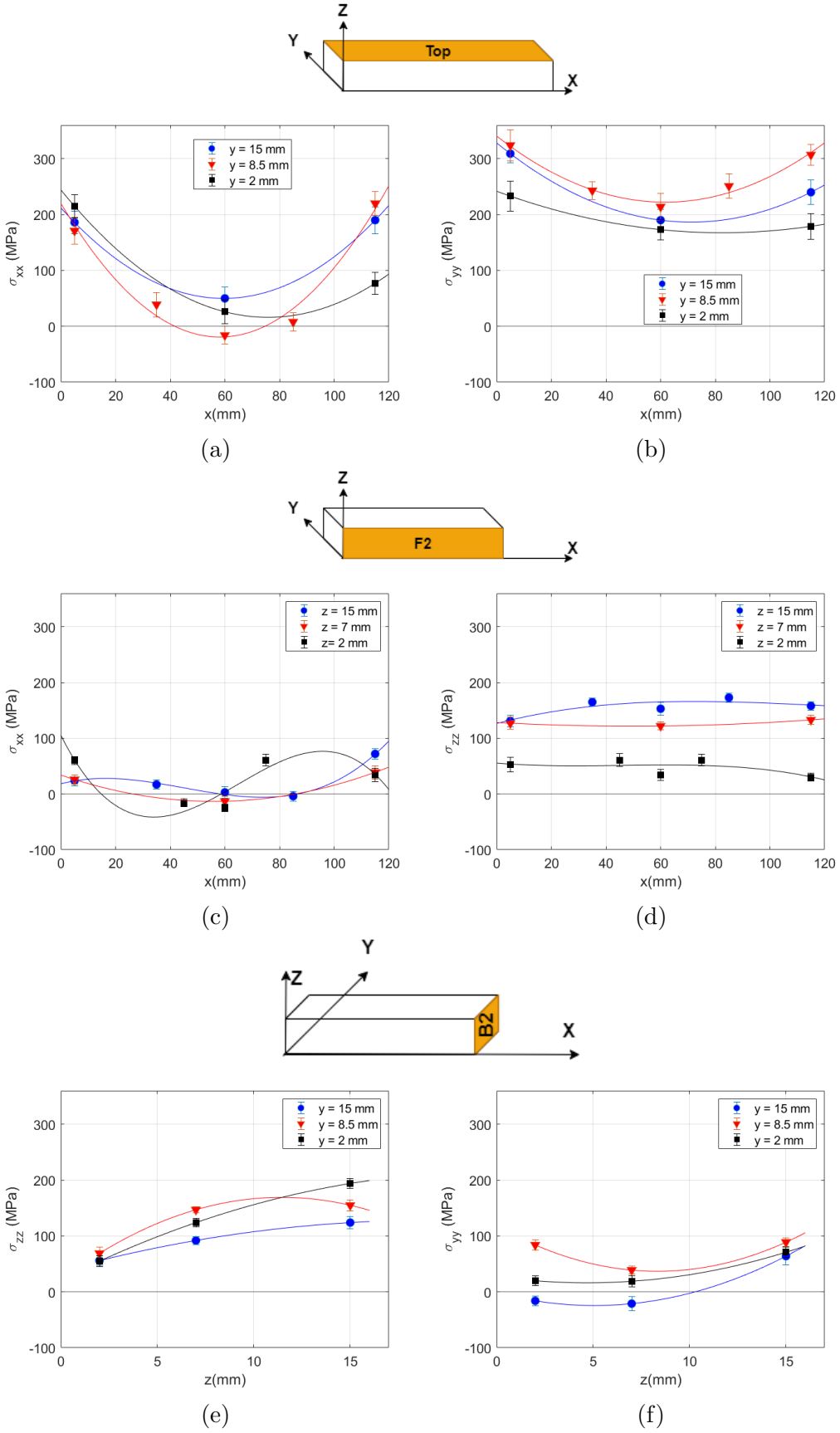

Figure 4.8: Residual stresses on the sample SS_T2 without the build plate: (a) top surface σ_{xx} (b) top surface σ_{yy} (c) lateral surface σ_{xx} (d) lateral surface σ_{zz} (e) base surface σ_{zz} (f) base surface σ_{yy}.

4.5.3 In-depth residual stresses on samples connected to the build plate

In this section, the in-depth residual stresses profiles are going to be presented. This analysis was made by the IHD method presented in Section 3.5. The profiles were determined in the position described in the schemes above the figures.

AISI 18Ni300, sample MAR_T

The residual stresses determined by incremental hole drilling method before the removal of the build plate are presented in Fig 4.9, for the sample MAR_T of AISI 18Ni300.

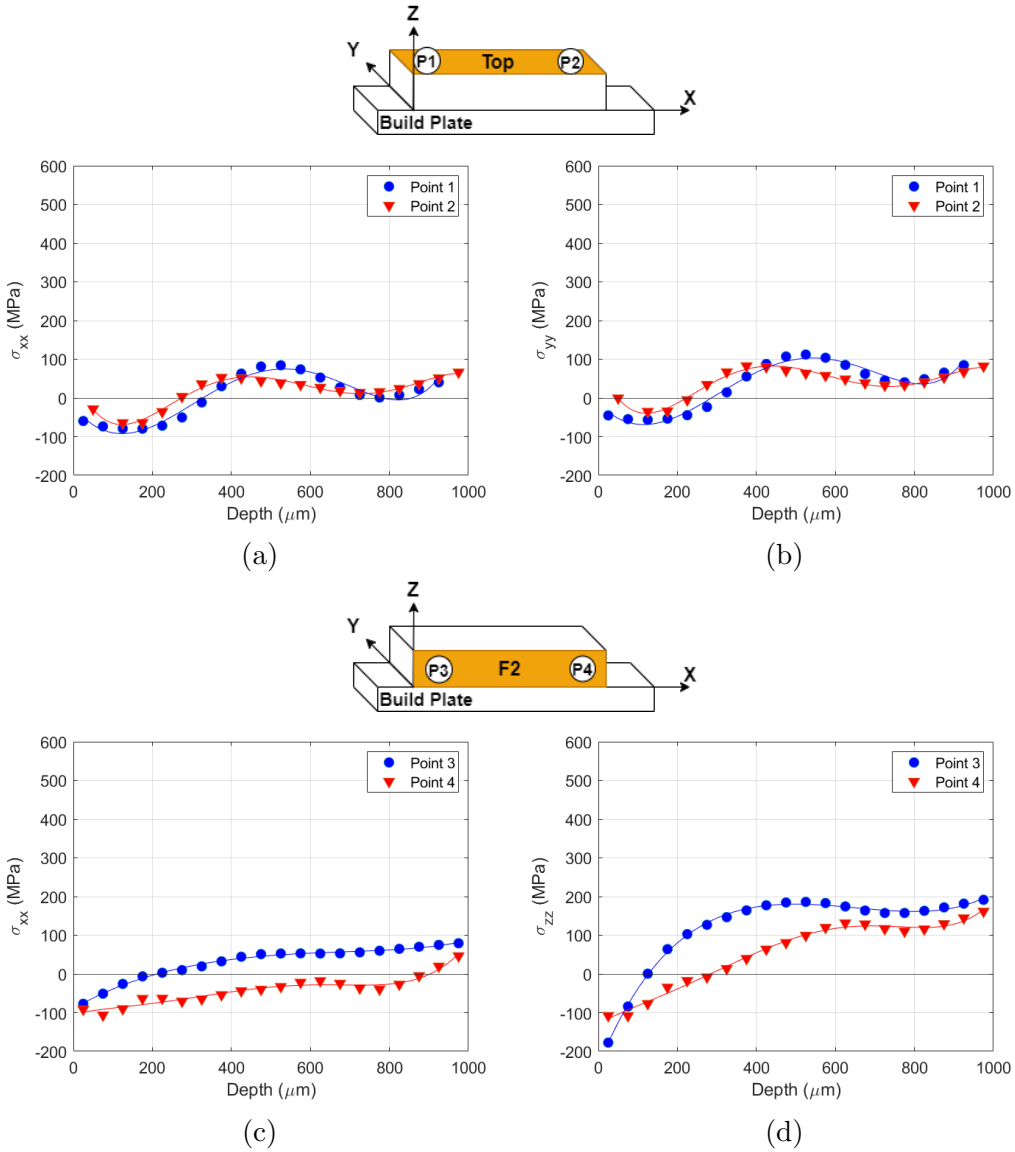

Figure 4.9: In-depth analysis of the residual stresses in the MAR_T sample using the incremental hole drilling method: (a) top surface σ_{xx} (b) top surface σ_{yy} (c) lateral surface σ_{xx} (d) lateral surface σ_{zz}.

As it can be observed in Fig 4.9a and Fig 4.9b, the values of the residual stresses for both points and directions are very similar. The residual stresses are compressive on the first 300-400

μm and after they become tensile and almost constant until the maximum depth reached.

The observed evolution over depth in the lateral surface shows that they all begin with compressive residual stresses and end with tensile residual stresses, Fig 4.9c and Fig 4.9d.

AISI 316L, sample SS_T2

In Fig 4.10 are presented the results of the residual stresses determined by incremental hole drilling method on the sample SS_T2 of AISI 316L still attached to the build plate.

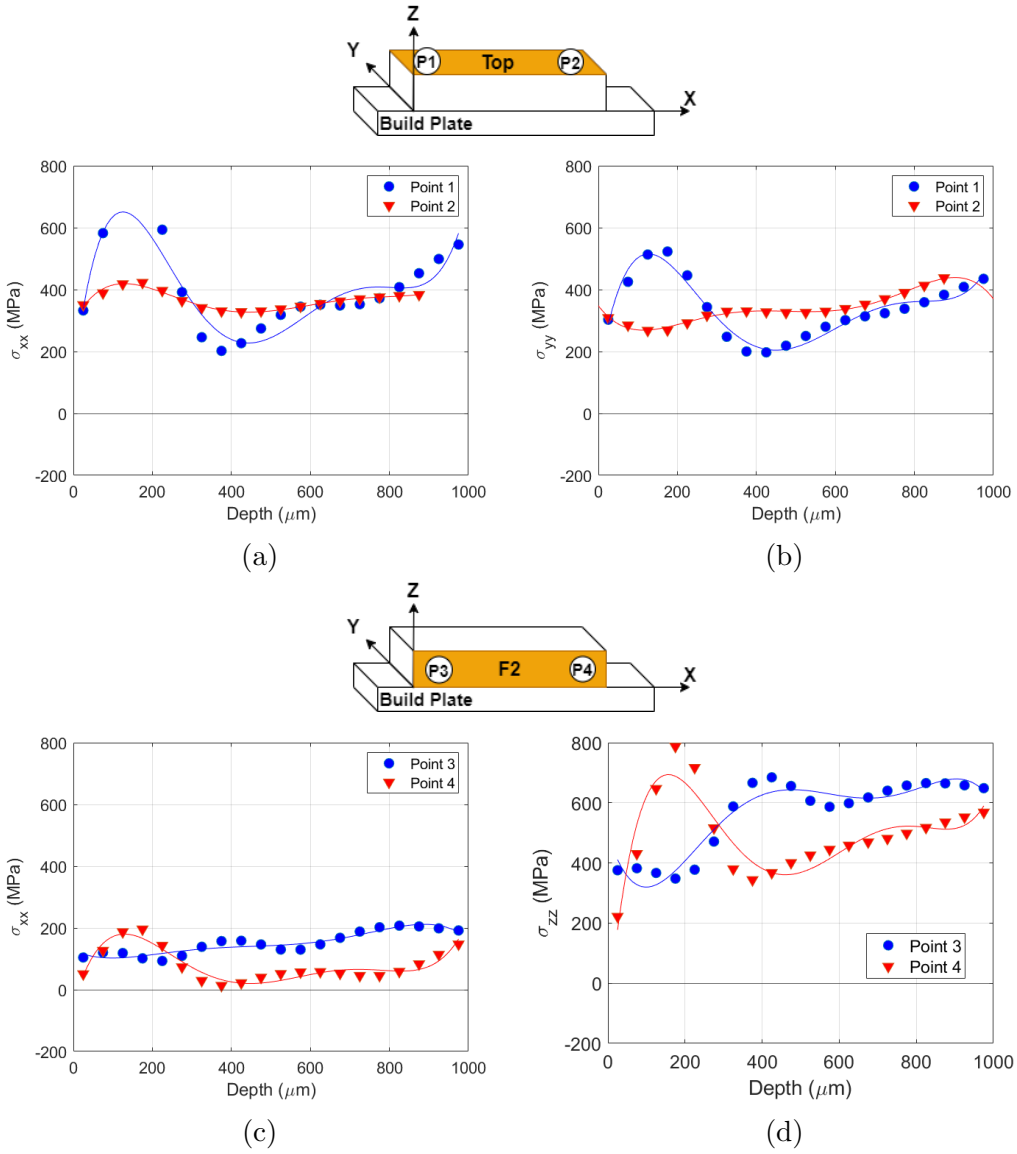

Figure 4.10: In-depth analysis of the residual stresses in the SS_T2 sample using the incremental hole drilling method: (a) top surface σ_{xx} (b) top surface σ_{yy} (c) lateral surface σ_{xx} (d) lateral surface σ_{zz}.

The residual stresses are tensile for P1 and P2. As it can be observed in Fig 4.10a and Fig 4.10b, the behaviour of the residual stresses for each point, P1 and P2, is different. For P1, there's a pronounced increase in the beginning and then some variation with depth, while for P2 the residual stresses are almost constant, in depth.

As presented in Fig 4.10c and Fig 4.10d, the residual stresses in the lateral surface are tensile. Initially there's a variation of the residual stresses until 400 μm. For higher depths, the residual stresses are almost constant. The profiles are different for each point, P3 and P4.

4.5.4 In-depth residual stresses after sample removal from the build plate

The study of the in-depth residual stresses distribution by XRD and by IHD was only performed on the biggest samples (SS_T2 and MAR_T). In this section, the results were obtained after the removal of the samples from the build plates. The results obtained by both methods are compared and discussed. For the XRD method, the in-depth analysis was performed on the top and on one of lateral surfaces - Table 4.6. For the IHD method, the new holes where drilled in the top and lateral surfaces - Table 4.7 .

The results obtained for the sample MAR_T can be seen in Fig 4.11 and for the sample SS_T2 the results obtained are on Fig 4.12.

Table 4.6: In sample positioning of the points where the analysis to determine the residual stresses by XRD method was made (Section 3.4).

Point	**Face**	**Coordinates (mm)**		
		X	**Y**	**Z**
P1	Top	60	8.5	17
P2	Frontal 2	60	0	7.5

Table 4.7: In sample positioning of the points where the analysis to determine the residual stresses by IHD method was made (Section 3.4).

Point	**Face**	**Coordinates (mm)**		
		X	**Y**	**Z**
P5	Frontal 2	40	0	7
P6	Frontal 2	80	0	7
P7	Frontal 1	60	17	7
P8	Top	40	8	16
P9	Top	80	8	16

AISI 18Ni300, sample MAR_T

The results obtained through XRD and IHD for the residual stresses in the sample MAR_T are presented in Fig 4.11. The in sample localisation of the points measured are graphically identified in the schemes above the graphics, for both techniques.

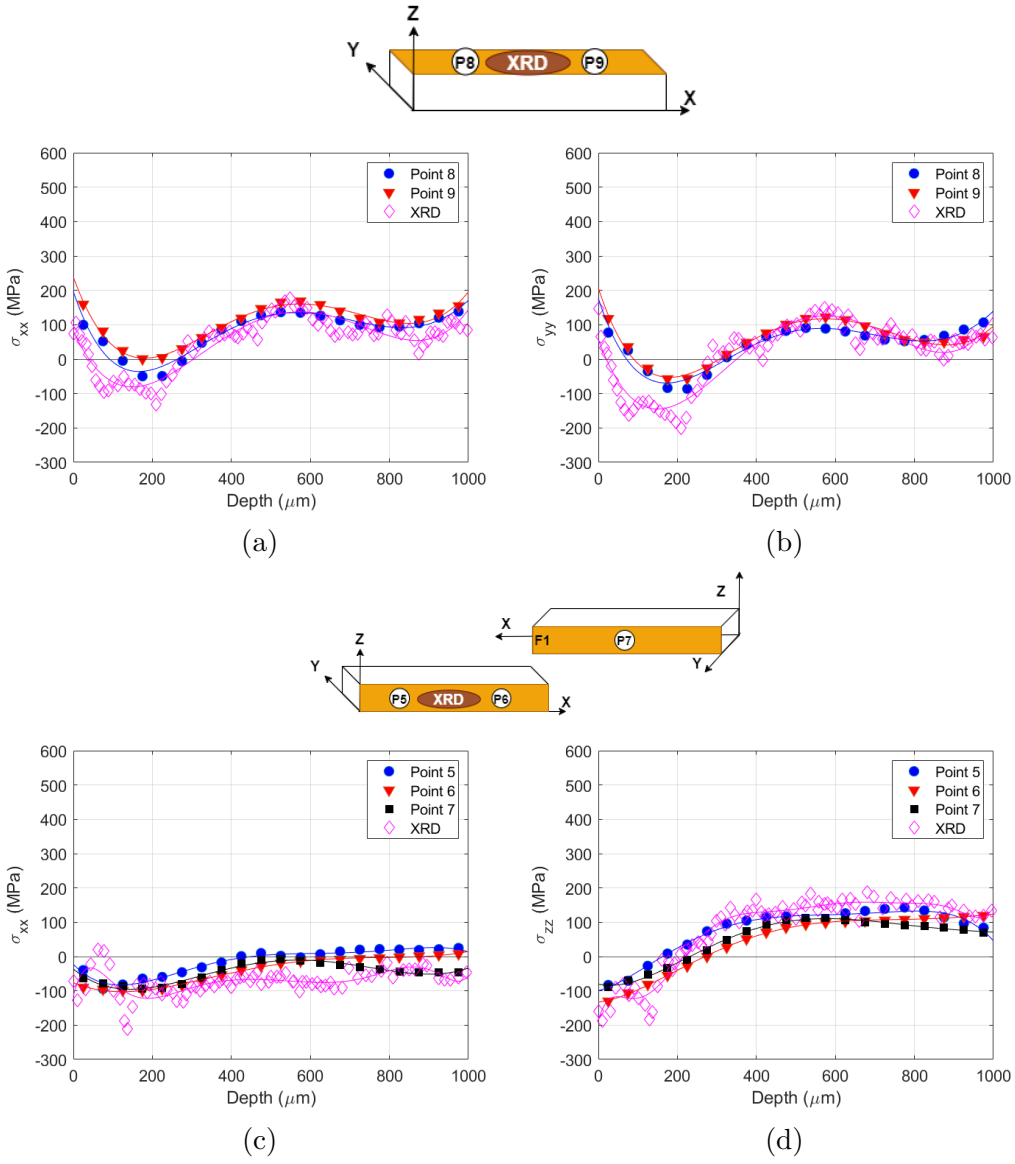

Figure 4.11: Residual stresses in-depth analysis, by XRD and by IHD in the MAR_T sample: (a) top surface σ_{xx} (b) top surface σ_{yy} (c) lateral surface σ_{xx} (d) lateral surface σ_{zz}.

As it can be seen in Fig 4.11, the residual stresses profiles obtained through both methods are similar.

The in-depth residual stresses for the top surface of the MAR_T sample are on Fig 4.11a and Fig 4.11b. The residual stresses are tensile in the first 50-100 μm, showing the maximum value at the surface. At depths between 50-100 μm and 200-300 μm the residual stresses are compressive. Between 300 μm until the maximum depth reached, the residual stresses are tensile and remain almost constant.

The residual stresses in the lateral surface of the sample MAR_T are on Fig 4.11c and Fig 4.11d. The residual stresses σ_{xx} are mostly compressive while, σ_{zz} are compressive until 200 μm, and after σ_{zz} are tensile. In the first 300 μm, there are some residual stress variations in both directions, but after, they can be consider almost constant.

AISI 316L, sample SS_T2

The results obtained through XRD and IHD for the residual stresses in the sample SS_T2 are presented in Fig 4.12. The in sample localisation of the points measured are graphically identified in the schemes above the graphics, for both techniques.

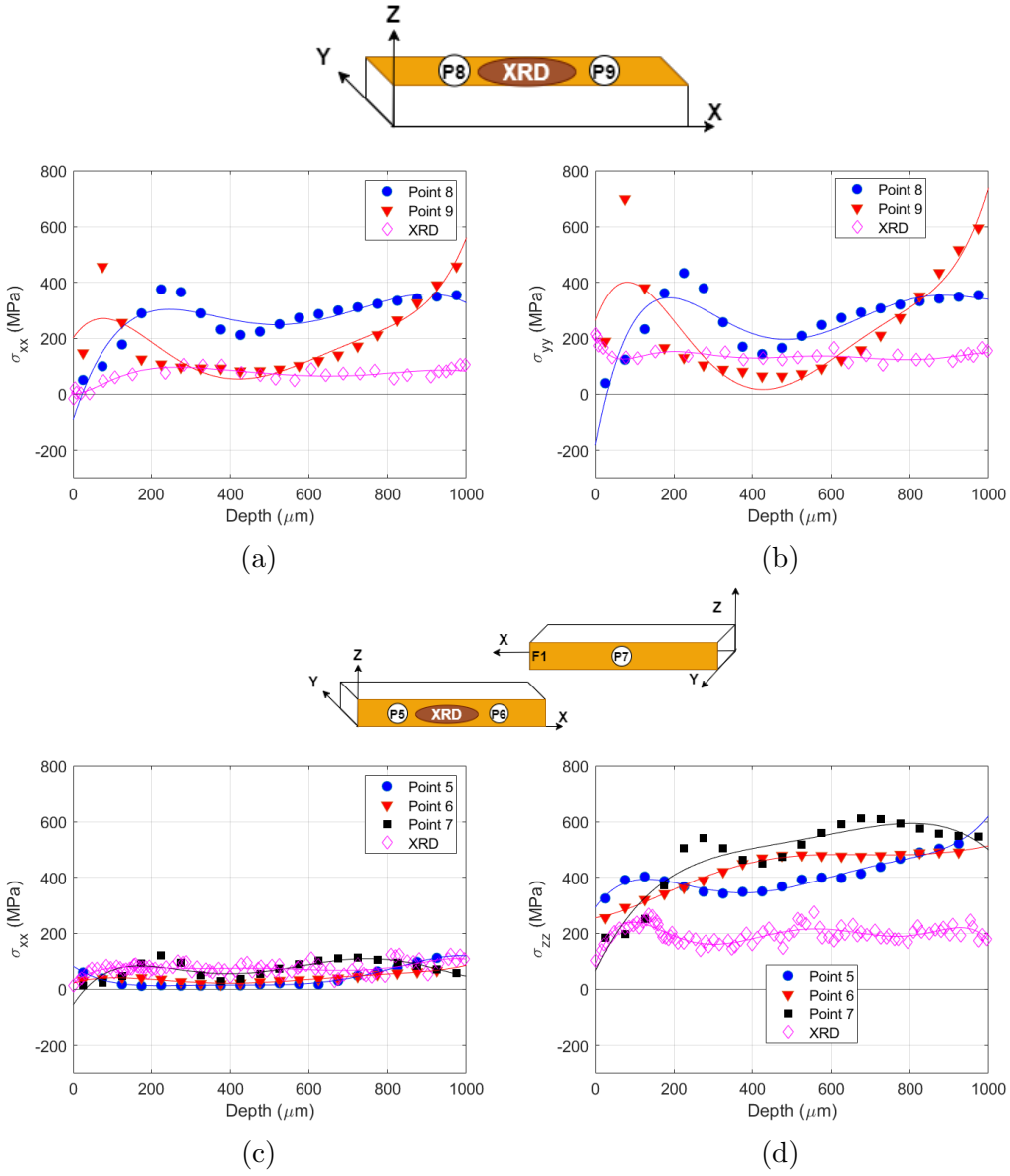

Figure 4.12: Residual stresses in-depth analysis, by XRD and by IHD in the SS_T2 sample: (a) top surface σ_{xx} (b) top surface σ_{yy} (c) lateral surface σ_{xx} (d) lateral surface σ_{zz}.

The residual stresses distribution presented in Fig 4.12 are tensile, nevertheless, the ones obtained by IHD are different from the ones obtained by XRD.

In the Fig 4.12a and Fig 4.12b, for the XRD, the residual stresses σ_{xx} increases in the first 100-200μm of depth, while σ_{yy} decreases. After reaching a depth of 200μm the residual stresses became almost constant and with similar patterns.

The residual stresses in the lateral surface of the sample SS_T2, Fig 4.12c and Fig 4.12d are tensile. For the XRD, both residual stresses σ_{xx} and σ_{zz} show a similar behaviour with depth: until 100 μm they increase in magnitude and after they are almost constant until the maximum depth measured. The values σ_{zz} are higher than the values of σ_{xx}.

The difference between the XRD and IHD determined residual stresses results could be explained by the fact that the IHD method is well established for ferritic steels, however due to the austenitic nature of the AISI 316L, the determined residual stresses may not be accurate. Another possible reason, is the plasticity effect. High residual stresses can lead to local yielding, due to stress concentration around the drilled hole, affecting the standard residual stress evaluation, which is based on linear plastic equations. This could result in an overestimation of the determined residual stresses by IHD [37].

Chapter 5

Conclusions and Future Work

5.1 Conclusions

The aim of the work developed in this dissertation had the goal of characterising SLM samples produced with two different materials (AISI 18Ni300 and AISI 316L) and with different geometries.

The microstructure presents scan tracks with elongated grains in the XY section (perpendicular to the building direction) while on the YZ section (parallel to the building direction) the structures are semi-circular. These structures are characteristic of samples produced by SLM.

The sample dimensions has negligible effect on the surface residual stresses, indicating that material characterisation could be performed in small samples. That could be useful during the first stages of research and development of new materials.

The residual stresses distribution in the samples surface was determined by the X-ray diffraction technique, before and after the removal of the samples from the build plate. The residual stresses in the top surface are tensile for both samples. In the lateral and base surfaces, the AISI 316L sample has tensile residual stresses while the AISI 18Ni300 has compressive residual stresses. Both results were expected based on previous studies made by other authors [29, 30]. The removal of the samples from the build plate by EDM has little influence on the residual stresses at the surface.

The in-depth residual stresses analysis after the removal of the samples from the build plate was performed with two different techniques: the X-ray diffraction and the incremental hole drilling. For the AISI 18Ni300 the results for both methods in each surface have almost the same distribution. For the AISI 316L, the results obtained by IHD are higher than the ones obtained by XRD. Overall, for the XRD method, the residual stresses after a depth of 200-400 μm remain almost constant until the maximum depth reached.

The influence of the build plate in the in-depth residual stresses analysis was studied by IHD method and no major differences were observed for the AISI 18Ni300 material. For the AISI 316L, the constrains in the application of the IHD method limits the conclusion about the influence of the build plate.

5.2 Future Work

Having taken into account the results obtained and the problems found during this work, it would be interesting to make a study focused on the AISI 316L material and the limitations of using the incremental hole drilling method in certain conditions, under high stresses close to the onset of plasticity.

SLM produced parts, usually have poor surface quality and depending on the requirements, it is also common to machine the surfaces to achieve fine tolerances and finish fine features, surfaces and holes. Therefore, for both materials, AISI 316L and AISI 18Ni300, a study on the machining parameters of the finishing operations and its influence on the mechanical characteristics should be made. Which is important in the application of these materials in various industries.

Appendix A

Appendix Title

A.1 Residual Stresses

A.1.1 Surface residual stresses of the AISI 18Ni300 maraging steel sample MAR_T

The residual stresses in the lateral surface of the sample MAR_T while still attached to the build plate are showed in Fig A.1 and the residual stresses in the same lateral surface, after the removal of the sample of the build plate are presented in Fig A.2.

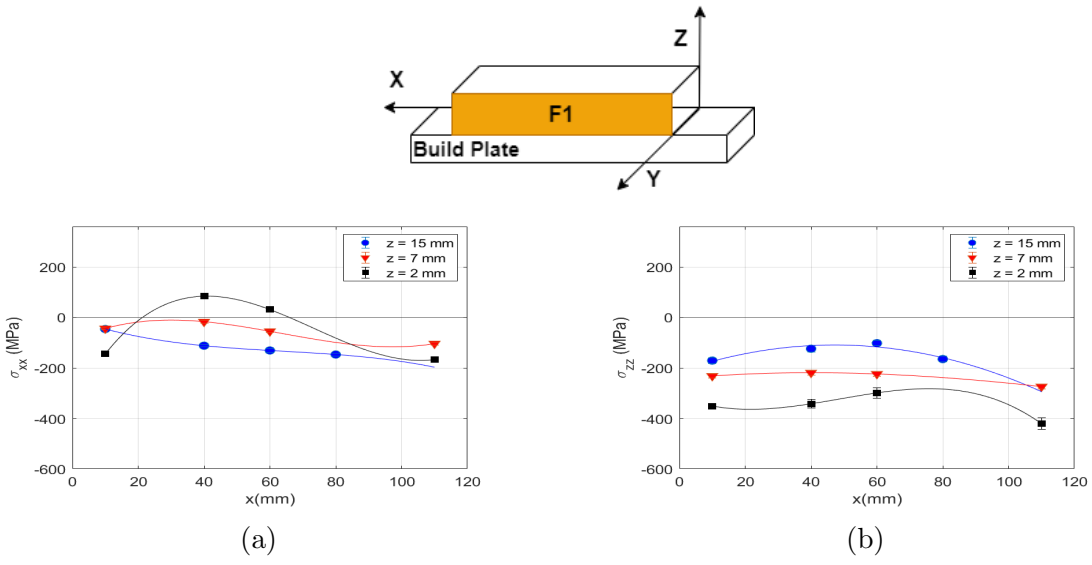

(a) (b)

Figure A.1: Residual stresses on the sample MAR_T before build plate removal: (a) Lateral surface σ_{xx} (b) Lateral surface σ_{zz}

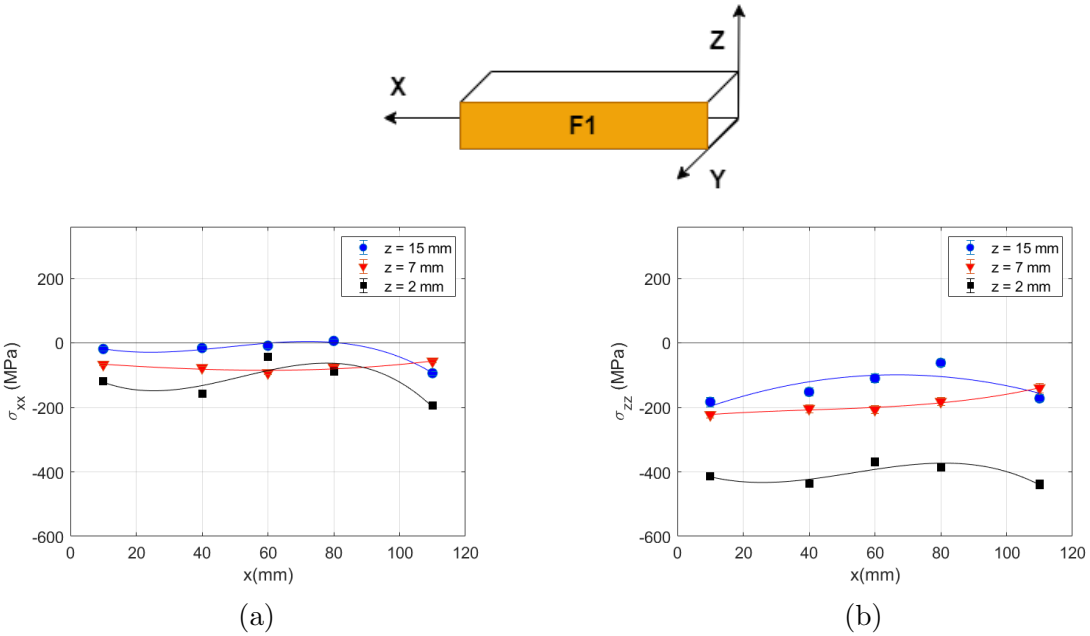

Figure A.2: Residual stresses on the sample MAR_T after build plate removal: (a) Lateral surface σ_{xx} (b) Lateral surface σ_{zz}

A.1.2 Surface residual stresses of the AISI 18Ni300 maraging steel sample MAR_0

The residual stresses in the sample MAR_0 while still attached to the build plate are showed in Fig A.3 and the residual stresses, after the removal of the sample of the build plate are presented in Fig A.4.

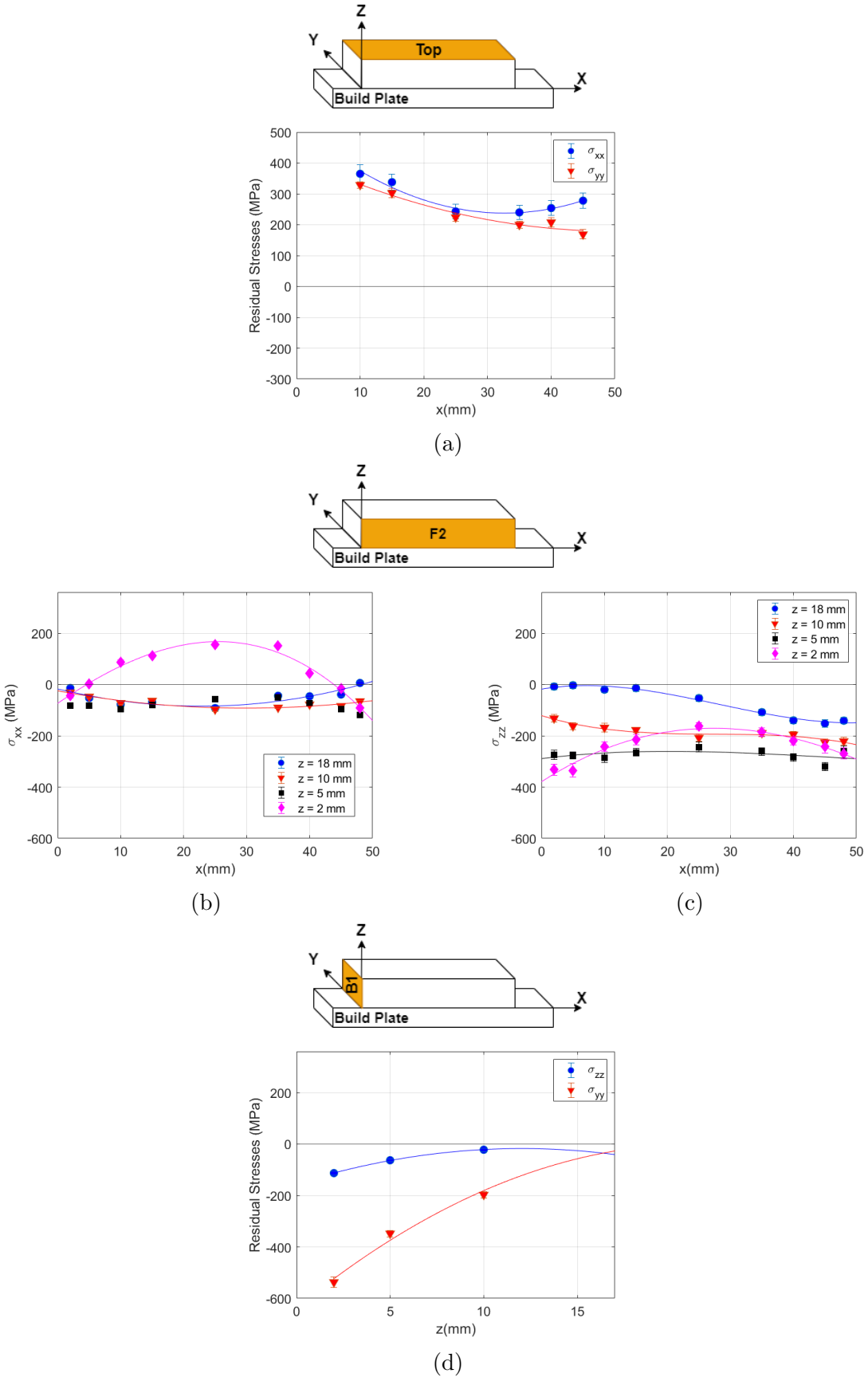

Figure A.3: Residual stresses on the sample MAR_0 before build plate removal: (a) Top surface σ_{xx} and σ_{yy} (b) Lateral surface σ_{xx} (c) Lateral surface σ_{zz} (d) Base surface σ_{zz} and σ_{yy}

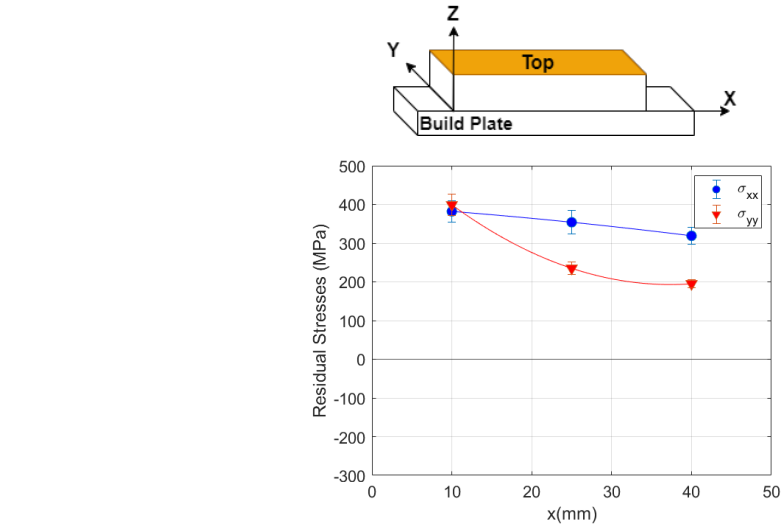

(a)

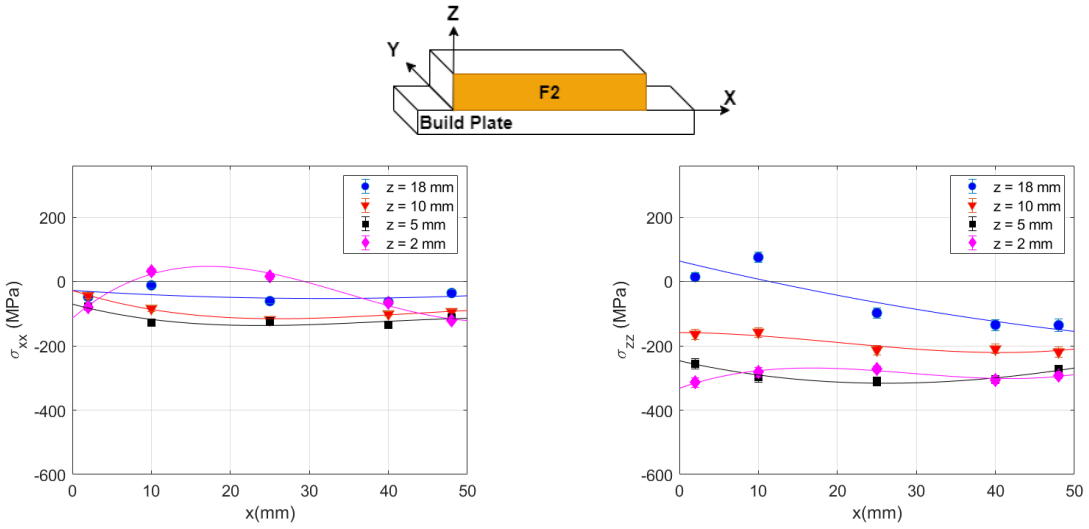

(b) (c)

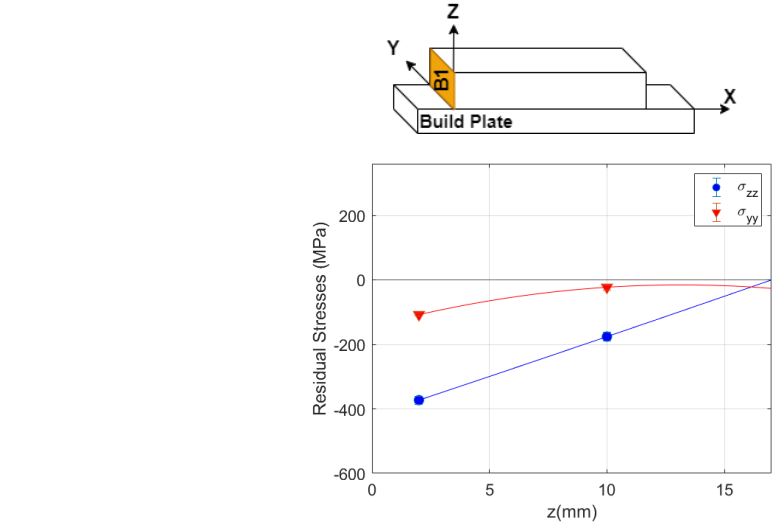

(d)

Figure A.4: Residual stresses on the sample MAR_0 after build plate removal: (a) Top surface σ_{xx} and σ_{yy} (c) Lateral surface σ_{xx} (d) Lateral surface σ_{zz} (e) Base surface σ_{zz} and σ_{yy}

A.1.3 Surface residual stresses of the AISI 316L stainless steel sample SS_02

The residual stresses in the sample SS_02 while still attached to the build plate are showed in Fig A.5 and Fig A.6 and the residual stresses, after the removal of the sample of the build plate are presented in Fig A.7 and Fig A.8.

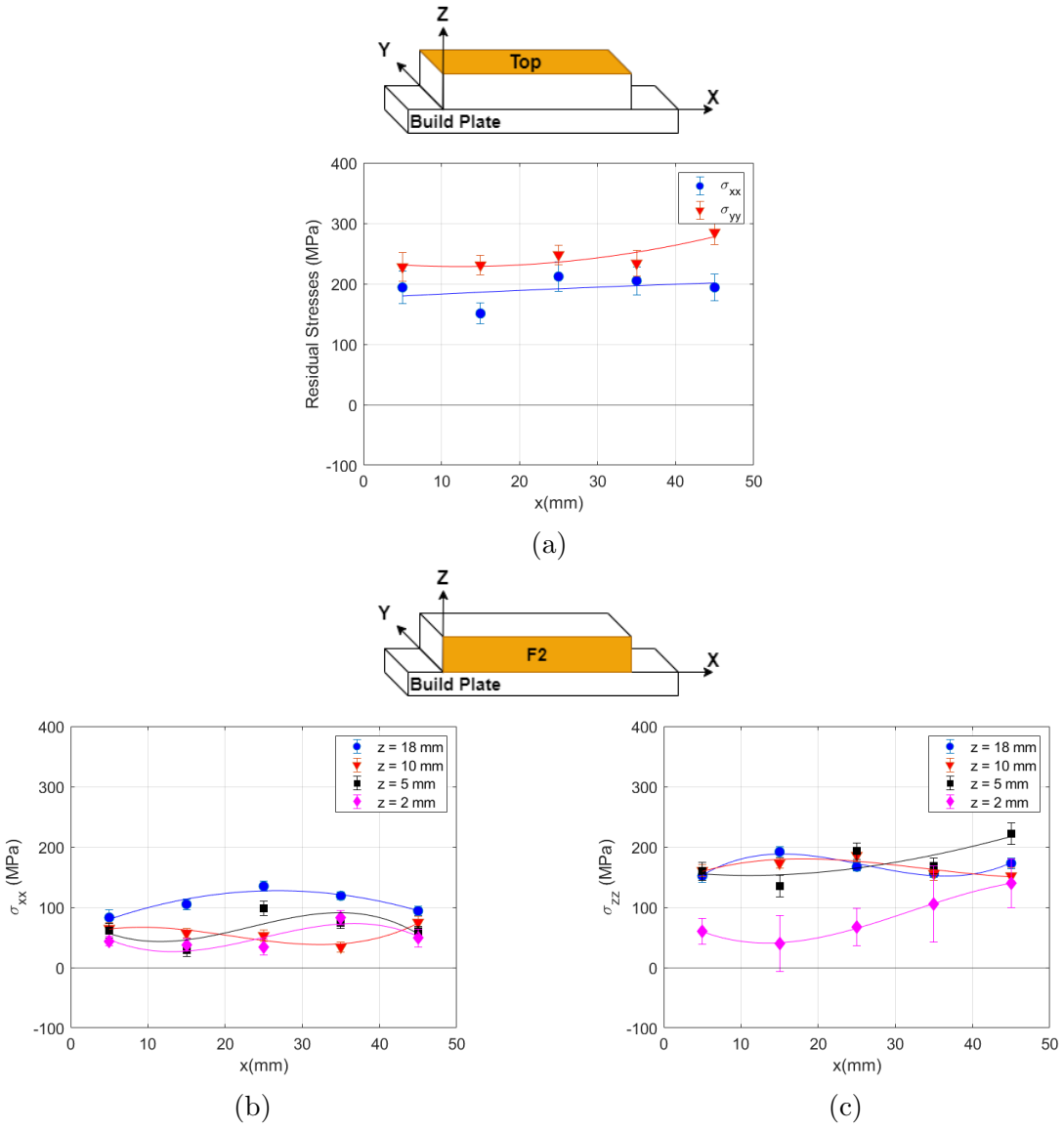

Figure A.5: Residual stresses on the sample SS_02 before build plate removal: (a) top surface σ_{xx} and σ_{yy} (b) lateral surface Frontal 2 σ_{xx} (c) lateral surface Frontal 2 σ_{zz}

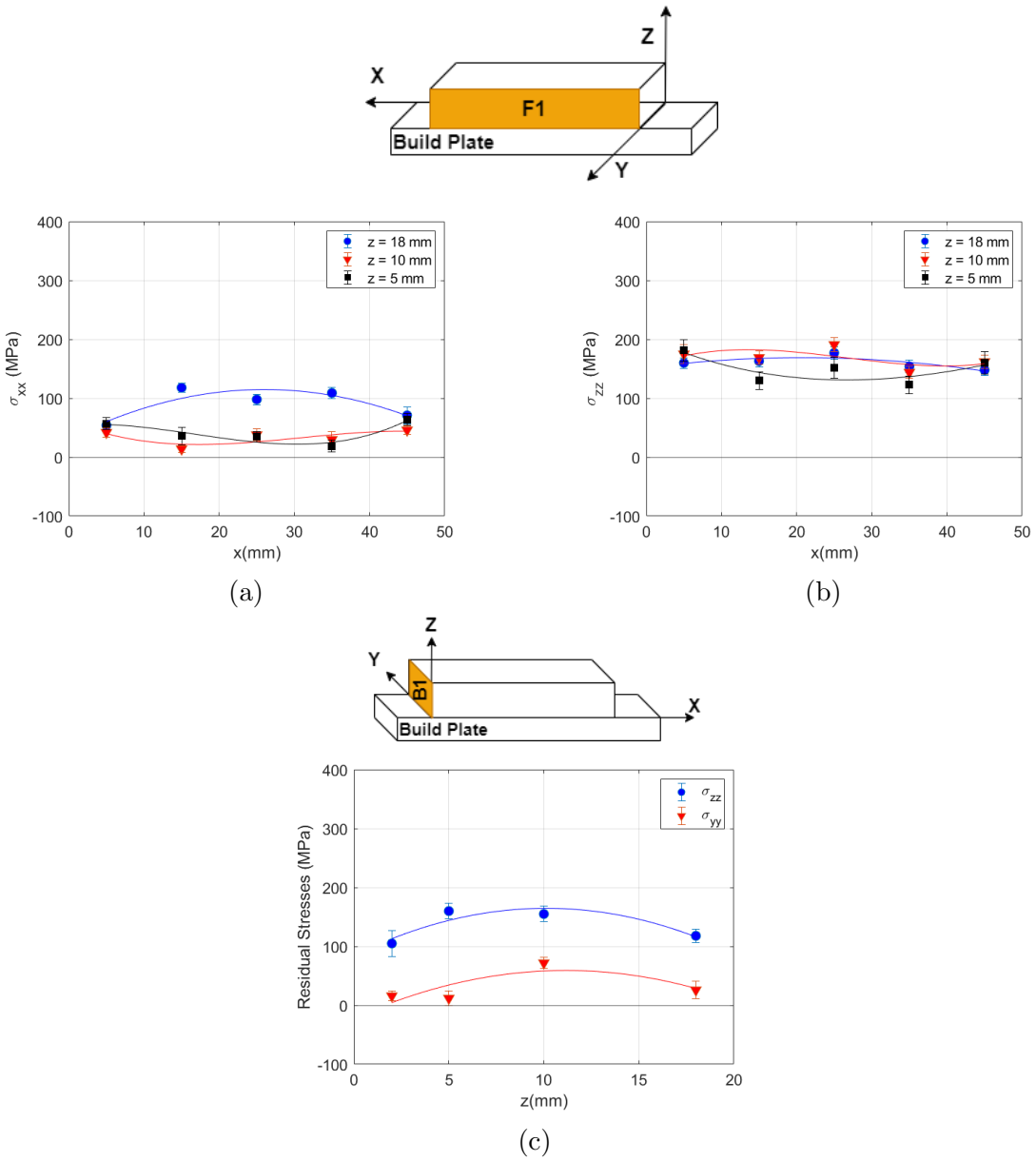

Figure A.6: Residual stresses on the sample SS_02 before build plate removal: (a) lateral surface Frontal 1 σ_{xx} (b) lateral surface Frontal 1 σ_{zz} (c) base surface σ_{zz} and σ_{yy}

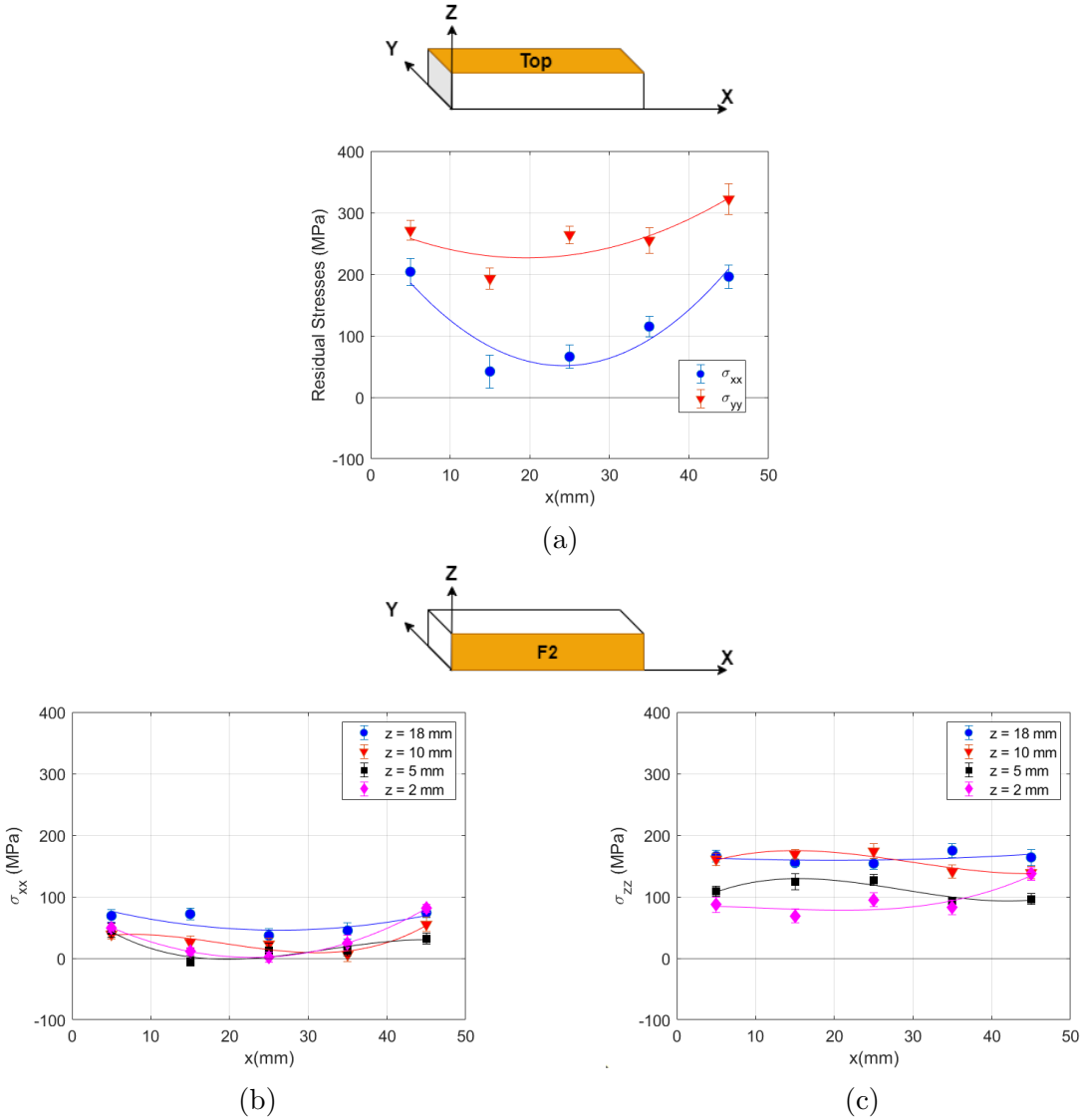

Figure A.7: Residual stresses on the sample SS_02 after build plate removal: (a) top surface σ_{xx} and σ_{yy} (b) lateral surface Frontal 2 σ_{xx} (c) lateral surface Frontal 2 σ_{zz}

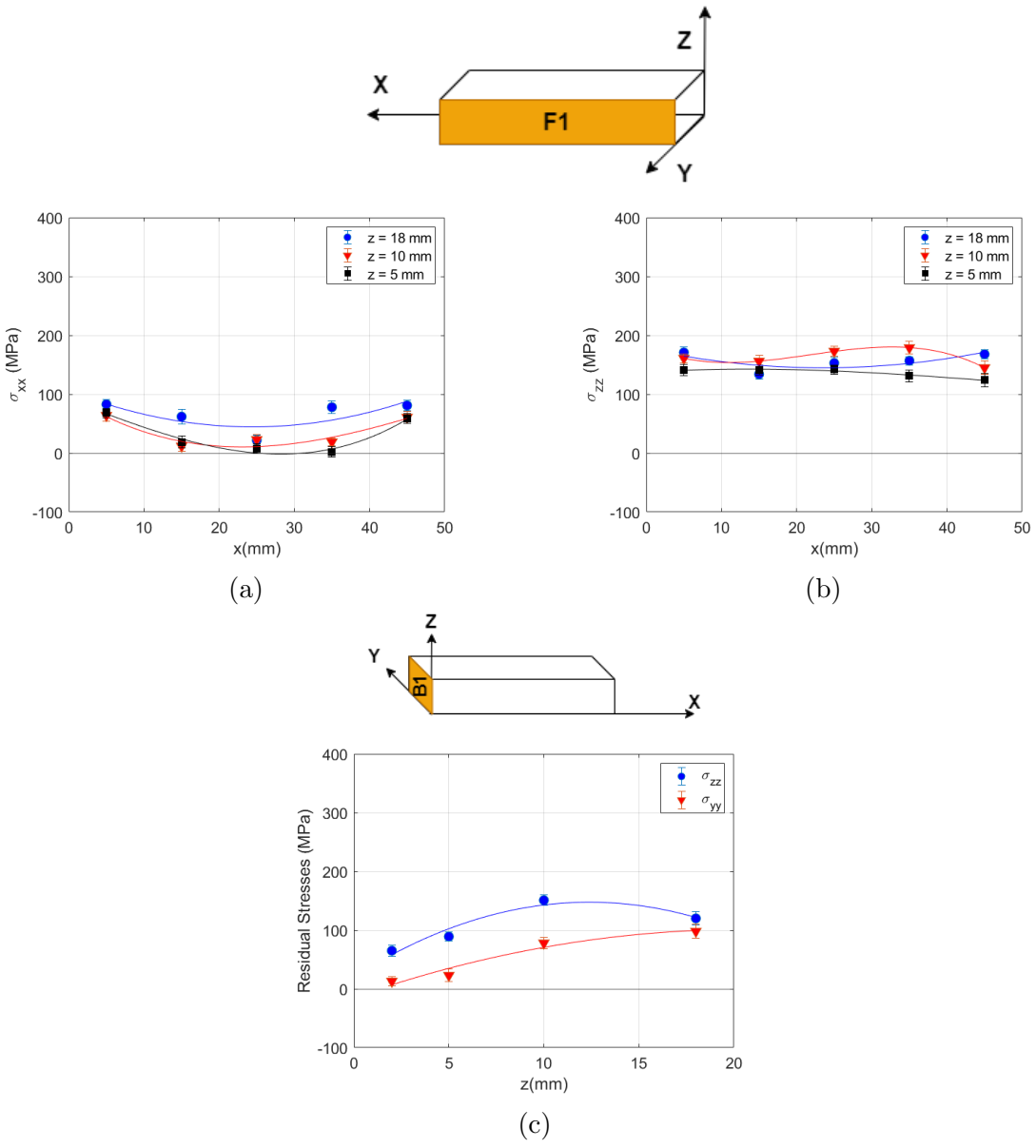

Figure A.8: Residual stresses on the sample SS_02 after build plate removal: (a) lateral surface Frontal 1 σ_{xx} (b) lateral surface Frontal 1 σ_{zz} (c) base surface σ_{zz} and σ_{yy}

Bibliography

[1] "ISO/TC 261". *"ISO/ASTM 52900 Additive manufacturing — General principles — Terminology"*. (accessed: 22.09.2020).

[2] Abbas Razavykia et al. 'An Overview of Additive Manufacturing Technologies—A Review to Technical Synthesis in Numerical Study of Selective Laser Melting'. In: *Materials* 13.17 (2020), p. 3895. ISSN: 1996-1944. DOI: 10.3390/ma13173895.

[3] Karel Kellens et al. 'Environmental Dimensions of Additive Manufacturing: Mapping Application Domains and Their Environmental Implications'. In: *Journal of Industrial Ecology* 21.S1 (2017), S49–S68. ISSN: 1088-1980. DOI: 10.1111/jiec.12629. URL: https://onlinelibrary.wiley.com/doi/pdf/10.1111/jiec.12719.

[4] Nesma T. Aboulkhair et al. '3D printing of Aluminium alloys: Additive Manufacturing of Aluminium alloys using selective laser melting'. In: *Progress in Materials Science* 106 (2019), p. 100578. ISSN: 0079-6425. DOI: 10.1016/j.pmatsci.2019.100578.

[5] H. Bikas, P. Stavropoulos and G. Chryssolouris. 'Additive manufacturing methods and modelling approaches: a critical review'. In: *The International Journal of Advanced Manufacturing Technology* 83.1-4 (2016), pp. 389–405. ISSN: 0268-3768. DOI: 10.1007/s00170-015-7576-2. URL: https://link.springer.com/content/pdf/10.1007\%2Fs00170-015-7576-2.pdf.

[6] *SLM and the patent rights monopoly*. URL: https://designandmotion.net/design-2/manufacturing-design/dmls-a-little-history/. (accessed: 10.12.2020).

[7] E. Yasa and J-P. Kruth. 'Microstructural investigation of Selective Laser Melting 316L stainless steel parts exposed to laser re-melting'. In: *Procedia Engineering* 19 (2011), pp. 389–395. ISSN: 1877-7058. DOI: 10.1016/j.proeng.2011.11.130. URL: https://doi.org/10.1016/j.proeng.2011.11.130.

[8] Yuchao Bai et al. 'Influence mechanism of parameters process and mechanical properties evolution mechanism of maraging steel 300 by selective laser melting'. In: *Materials Science and Engineering: A* 703 (2017), pp. 116–123. ISSN: 0921-5093. DOI: 10.1016/j.msea.2017.06.033.

[9] Lore Thijs. 'Microstructure and texture of metal parts produced by Selective Laser Melting'. PhD thesis. Ku LEUVEN.

[10] Chor Yen Yap et al. 'Review of selective laser melting: Materials and applications'. In: *Applied Physics Reviews* 2 (Dec. 2015), p. 041101. DOI: 10.1063/1.4935926.

[11] Ian Gibson. *Additive manufacturing technologies : 3D printing, rapid prototyping, and direct digital manufacturing*. New York, NY: Springer, 2015. ISBN: 978-1-4939-2113-3.

[12] Lore Thijs et al. 'Fine-structured aluminium products with controllable texture by selective laser melting of pre-alloyed AISI10Mg powder'. In: *Acta Materialia* 61.5 (2013), 1809–1819. DOI: 10.1016/j.actamat.2012.11.052. URL: http://dx.doi.org/10.1016/j.actamat.2012.11.052.

[13] Mohd Sanusi Abdul Aziz et al. 'Residual Stress and Deformation of Consolidated Structure Obtained by Layered Manufacturing Process'. In: 7.2 (2013), pp. 244–256. ISSN: 1881-3054. DOI: 10.1299/jamdsm.7.244. URL: https://www.jstage.jst.go.jp/article/jamdsm/7/2/7_244/_pdf.

[14] M. Król and T. Tański. 'Surface Quality Research for Selective Laser Melting of Ti-6Al-4V Alloy'. In: *Archives of Metallurgy and Materials* 61.3 (Sept. 2016), pp. 1291–1296. DOI: 10.1515/amm-2016-0213. URL: https://doi.org/10.1515/amm-2016-0213.

[15] Nesma T. Aboulkhair et al. 'Reducing porosity in AISI10Mg parts processed by selective laser melting'. In: *Additive Manufacturing* 1-4 (2014), pp. 77–86. ISSN: 2214-8604. DOI: 10.1016/j.addma.2014.08.001.

[16] Rongshi Xiao and Xinyi Zhang. 'Problems and issues in laser beam welding of aluminum–lithium alloys'. In: *Journal of Manufacturing Processes* 16.2 (2014), pp. 166–175. ISSN: 1526-6125. DOI: 10.1016/j.jmapro.2013.10.005.

[17] B. Zhang, Y. Li and Q. Bai. 'Defect Formation Mechanisms in Selective Laser Melting: A Review'. In: *Chinese Journal of Mechanical Engineering* 30 (2017), pp. 515–527.

[18] Eric Jägle et al. 'Comparison of Maraging Steel Micro- and Nanostructure Produced Conventionally and by Laser Additive Manufacturing'. In: *Materials* 10.1 (2016), p. 8. ISSN: 1996-1944. DOI: 10.3390/ma10010008. URL: https://www.mdpi.com/1996-1944/10/1/8/pdf.

[19] K. Kempen et al. 'Microstructure and mechanical properties of Selective Laser Melted 18Ni-300 steel'. In: *Physics Procedia* 12 (2011), pp. 255–263. ISSN: 1875-3892. DOI: 10.1016/j.phpro.2011.03.033. URL: https://doi.org/10.1016/j.phpro.2011.03.033.

[20] Mariusz Król et al. 'Selective Laser Melting of 18NI-300 Maraging Steel'. In: *Materials* 13.19 (2020), p. 4268. ISSN: 1996-1944. DOI: 10.3390/ma13194268.

[21] *Martensite alloys*. URL: http://www.dierk-raabe.com/martensite-alloys-and-transformations/. (accessed: 19.12.2020).

[22] *Maraging steel M300 powder for additive manufacturing*. Renishaw. Sept. 2017. URL: www.renishaw.com/additive.

[23] Naoki Takata et al. 'Crystallographic Features of Microstructure in Maraging Steel Fabricated by Selective Laser Melting'. In: *Metals* 8.6 (2018), p. 440. ISSN: 2075-4701. DOI: 10.3390/met8060440. URL: https://www.mdpi.com/2075-4701/8/6/440/pdf.

[24] William F. Smith. *Princípios de ciência e engenharia de materiais*. Tít. orig. : Principles of materials science and engineering. Lisboa [etc.]: McGraw-Hill, 2007. ISBN: 972-8298-68-4.

[25] *Grade 316 Stainless Steel: Properties, Fabrication and Applications*. URL: https://www.azom.com/article.aspx?ArticleID=2868. (accessed: 20.12.2020).

[26] *SS 316L-0407 powder for additive manufacturing*. Renishaw. Apr. 2018. URL: www.renishaw.com/additive.

[27] *What is Residual Stress*. URL: https://www.twi-global.com/. (accessed: 22.09.2020).

[28] Viktor Hauk. *Structural and Residual Stress Analysis by Nondestructive Methods*. Elsevier, 1997. DOI: 10.1016/b978-0-444-82476-9.x5000-2. URL: https://doi.org/10.1016/b978-0-444-82476-9.x5000-2.

[29] Thomas Simson et al. 'Residual stress measurements on AISI 316L samples manufactured by selective laser melting'. In: *Additive Manufacturing* 17 (2017), pp. 183–189. ISSN: 2214-8604. DOI: 10.1016/j.addma.2017.07.007.

[30] Mugwagwa, Yadroitsev and Matope. 'Effect of Process Parameters on Residual Stresses, Distortions, and Porosity in Selective Laser Melting of Maraging Steel 300'. In: *Metals* 9.10 (2019), p. 1042. ISSN: 2075-4701. DOI: 10.3390/met9101042.

[31] J. Lu and Society for Experimental Mechanics (U.S.) *Handbook of Measurement of Residual Stresses*. Fairmont Press, 1996. ISBN: 9780132557382. URL: https://books.google.pt/books?id=VvtDAQAAIAAJ.

[32] *Test Method for Determining Residual Stresses by the Hole-Drilling Strain-Gage Method*. DOI: 10.1520/e0837-20. URL: https://doi.org/10.1520/e0837-20.

[33] *Buehler Sum-Met : the science behind materials preparation ; a guide to materials preparation and analysis*. Lake Bluff, Il: Buehler, 2004. ISBN: 0-9752898-0-2.

[34] *Test Methods for Vickers Hardness and Knoop Hardness of Metallic Materials*. DOI: 10.1520/e0092-17. URL: http://dx.doi.org/10.1520/E0092-17.

[35] *Vickers test procedure*. URL: https://www.emcotest.com/en/the-world-of-hardness-testing/hardness-know-how/theory-of-hardness-testing/vickers-52/vickers-test-procedure-185/. (accessed: 07.06.2021).

[36] Shahir Yusuf et al. 'Investigation on Porosity and Microhardness of 316L Stainless Steel Fabricated by Selective Laser Melting'. In: *Metals* 7.2 (2017), p. 64. ISSN: 2075-4701. DOI: 10.3390/met7020064. URL: https://doi.org/10.3390/met7020064.

[37] J. P. Nobre, M. Kornmeier and B. Scholtes. 'Plasticity Effects in the Hole-Drilling Residual Stress Measurement in Peened Surfaces'. In: *Experimental Mechanics* 58.2 (2018), pp. 369–380. ISSN: 0014-4851. DOI: 10.1007/s11340-017-0352-5.